

Intraseasonal descriptors and extremes in South African rainfall. Part II: Summer teleconnections across multiple timescales

Ullah, A., Pohl, B., Pergaud, J., Dieppois, B. & Rouault, M

Published PDF deposited in Coventry University's Repository

Original citation:

Ullah, A, Pohl, B, Pergaud, J, Dieppois, B & Rouault, M 2023, 'Intraseasonal descriptors and extremes in South African rainfall. Part II: Summer teleconnections across multiple timescales', *International Journal of Climatology*.

<https://doi.org/10.1002/joc.8059>

DOI 10.1002/joc.8059

ISSN 0899-8418

ESSN 1097-0088

Publisher:



Wiley

© 2023 The Authors. *International Journal of Climatology* published by John Wiley & Sons Ltd on behalf of Royal Meteorological Society.

This is an open access article under the terms of the Creative Commons Attribution-NonCommercial-NoDerivs License, which permits use and distribution in any medium, provided the original work is properly cited, the use is non-commercial and no modifications or adaptations are made.

RESEARCH ARTICLE

Intraseasonal descriptors and extremes in South African rainfall. Part II: Summer teleconnections across multiple timescales

Asmat Ullah¹  | Benjamin Pohl¹  | Julien Pergaud¹ | Bastien Dieppois² | Mathieu Rouault³

¹Centre de Recherches de Climatologie, UMR 6282 Biogéosciences, CNRS/ Université de Bourgogne Franche-Comté, Dijon, France

²Centre for Agroecology, Water and Resilience, Coventry University, Coventry, UK

³Nansen Tutu Center for Marine Environmental Research, Department of Oceanography, University of Cape Town, Cape Town, South Africa

Correspondence

Asmat Ullah, Laboratoire Biogéosciences, Université de Bourgogne, 6 Boulevard Gabriel, 21000 Dijon, France.
Email: asmat-786@hotmail.com

Funding information

I-SITE Bourgogne Franche-Comté Junior Fellowship IMVULA, Grant/Award Number: AAP2-JF-06; Alliance Programme 2020, Grant/Award Number: 608081922

Abstract

Extreme events contribute significantly to rainfall variability in semi-arid regions like South Africa. Here, following the definition of a novel typology of rainfall extremes, disentangling large- and small-scale events in Part I, we use quality-controlled observational databases in South Africa, the ERA5 reanalysis and satellite estimates TRMM-3B42 to examine the relationship between these two types of rainfall extremes and different modes of climate variability at various timescales. At low frequencies, rainfall extremes are assessed at interannual (IV: 2–8 years) and quasi-decadal (QDV: 8–13 years) timescales, which are primarily associated with the El Niño–Southern Oscillation (ENSO) and the Interdecadal Pacific Oscillation (IPO), respectively. At subseasonal timescales, the typology of rainfall extremes is analysed depending on the synoptic configurations, as inferred by seven convective regimes including tropical temperate troughs (TTTs: 3–7 days), and the intraseasonal variability associated with the Madden–Julien Oscillation (MJO: 30–60 days). At the IV timescale, the occurrence of large-scale extremes is substantially higher during its wet phases thereby suggesting a 400% rise in the occurrence of large-scale extremes as compared to its dry phases. At the QDV timescale, variability mostly relates to the modulation of small-scale extremes during its wet phases. Teleconnections with global sea surface temperature (SST) confirm that La Niña conditions favour overall wet conditions and extremes in South Africa. The numbers of large-scale extremes are consistently related to warmer SSTs in the North Atlantic, while their link with warmer Indian and tropical South Atlantic oceans is found to be statistically independent of the state of ENSO. At the subseasonal timescales, large-scale extremes largely occur during three out of the seven convective regimes identified in the southern African region whereas small-scale extremes are nearly equiprobable during all convective

This is an open access article under the terms of the [Creative Commons Attribution-NonCommercial-NoDerivs](https://creativecommons.org/licenses/by-nc-nd/4.0/) License, which permits use and distribution in any medium, provided the original work is properly cited, the use is non-commercial and no modifications or adaptations are made.

© 2023 The Authors. *International Journal of Climatology* published by John Wiley & Sons Ltd on behalf of Royal Meteorological Society.

regimes. The occurrence of large-scale extremes during continent-rooted TTT is further enhanced during the locally wet phases of the MJO and is symmetrically weakened during its dry phases.

KEYWORDS

atmospheric convection, El Niño–Southern Oscillation, Interdecadal Pacific Oscillation, large-scale and small-scale extremes, Madden–Julien Oscillation, rainfall, South Africa, tropical temperate troughs

1 | INTRODUCTION

Hydrometeorological extremes such as droughts and floods are of crucial importance for human society. Such extremes are likely to be more frequent and intense at and above 1.5 C global warming levels (Donat et al., 2016). Several studies have explored the response of rainfall extremes to climate change in South Africa (Engelbrecht et al., 2013; Mason et al., 1999; Mason & Joubert, 1997; Pinto et al., 2016; Shongwe et al., 2009). Pohl et al. (2017) pointed out a significant decrease in the number of rainy days and an increase in their intensity, in line with the Clausius–Clapeyron relation linking air moisture to temperature. Similar results are drawn using convection-permitting models at the regional scales (Jackson et al., 2020; Kendon et al., 2017, 2019; Senior et al., 2021). However, despite its primary importance in predicting potential climate risks in sectors such as agriculture and hydropower (Conway et al., 2015, 2017), we currently know very little about how these extreme rainfall events are distributed during the austral summer season at the synoptic, intraseasonal, interannual and decadal timescale.

During the main rainy season from November to February (hereinafter NDJF), rainfall exhibits three significant timescales of variability related to the distinct modes of Pacific variability over the twentieth century: interannual (IV: 2–8 years), quasi-decadal (QDV: 8–13 years) and interdecadal variations (IDV: 15–28 years; Dieppois et al., 2016, 2019). Hereafter, the IV, QDV and IDV timescales are referred to as low-frequency timescales of variability.

At the IV timescale, rainfall variability is strongly modulated by El Niño–Southern Oscillation (Dieppois et al., 2015; Nicholson & Kim, 1997; Washington & Preston, 2006). Typically, El Niño conditions tend to favour dry summers while La Niña led to above-normal rainfall in South Africa. However, the relationship between ENSO and rainfall is not systematic, since not every El Niño event leads to dry conditions over the region (Reason & Jagadheesha, 2005; Rouault & Richard, 2004). This could be due to interferences with the Angola Low

(Lyon & Mason, 2007; Pascale et al., 2019) or the Subtropical Indian Ocean Dipole (SIOD; Hoell & Cheng, 2018). Moreover, recent changes in the number of dry spells and wet days in southern Africa could relate to a combined influence of ENSO, the Southern Annular Mode (SAM), SIOD and the Botswana High (Thoithi et al., 2020).

At the quasi-decadal timescale, rainfall variability mostly relates to the Interdecadal Pacific Oscillation (IPO; Dieppois et al., 2016, 2019). IPO exhibits ENSO-like sea surface temperature (SST) patterns, shifting the Walker-circulation zonally and resulting in an eastward shift of the South Indian Convergence Zone (SICZ), thus modifying the preferential location and intensity of tropical temperate troughs (TTTs; Pohl et al., 2018). However, how much interannual and decadal timescales of climate variability affect the likelihood and the total rainfall variability associated with extreme rainfall events is not known.

At the subseasonal timescales, austral summer rainfall variability is strongly associated with synoptic scale (i.e., 1–7 days), notably the convective cloud bands widely known as TTTs (Fauchereau et al., 2009; Hart et al., 2010; Macron et al., 2014; Todd et al., 2004; Todd & Washington, 1999; Vigaud et al., 2012; Washington & Todd, 1999). TTTs are responsible for 30%–60% of summer rainfall in southern Africa (Hart et al., 2013; Macron et al., 2014; Reason et al., 2006). TTTs are oriented from northwest to southeast and are the results of interactions between transient perturbations in the midlatitudes and tropical convection (Hart et al., 2010; James et al., 2020; Macron et al., 2014), thereby linking the Tropics to the temperate latitudes. Other notable rain-bearing systems of summer rainfall are mesoscale convective complexes (MCCs; Blamey & Reason, 2013), squall lines (Rouault et al., 2002), tropical storms (Fitchett & Grab, 2014; Malherbe et al., 2012, 2014; Reason & Keibel, 2004) and cut-off lows (Favre et al., 2013).

Austral summer rainfall also varies at intraseasonal timescales (i.e., 30–60 days), where the Madden–Julien Oscillation (MJO) is the dominant mode of variability (Madden & Julian, 1994; Zhang, 2005). The MJO is characterized as an eastward propagation of large-scale

convective clusters in the Tropics, which recur every 30–60 days (Madden & Julian, 1994; Zhang, 2005), and have overarching effects on rainfall patterns across the world (Donald et al., 2006; Zhang, 2005). Several cohort studies investigated the connection between MJO and precipitation over South Africa in various dimensions. Pohl et al. (2007) were the first to point out the influence of the MJO on summer rainfall variability across southern Africa. Their results were further completed and confirmed by Oettli et al. (2014). Grimm and Reason (2015) assessed the intraseasonal teleconnections between South America and South African rainfall and show that these teleconnections are caused by eastward propagating wave trains, which are modulated by the convective activity of MJO over tropical South America. Puaud et al. (2017) confirmed and further investigated these teleconnections and suggest that at the intraseasonal timescale, the covariability is related to the modulations of large-scale atmospheric convection over South America, and then over tropical southern Africa after around 10 days. Grimm (2019) suggested the strongest convective activity over South Africa relate to MJO phase #7 and noted positive anomalies in MJO phase #6. This study highlighted that the connection between MJO and regional convective activity is not very strong (although significant), thereby confirming the conclusions of Pohl et al. (2009) for southern Africa. This is probably because at least part of the MJO influence is indirect, exerted through the MJO-related anomalies over South America (Grimm, 2019) or through modulation of moisture fluxes and moisture convergence over Africa (Pohl et al., 2007). Silvério and Grimm (2022) proposed a precipitation index for southern Africa and suggest that the enhancement of precipitation in Mozambique is preceded by enhanced precipitation over South Africa.

In terms of the combined influence of synoptic-scale convective regimes and intraseasonal variability associated with MJO, no discernible relation could be found between MJO and the occurrence of TTTs (Pohl et al., 2009) but Hart et al. (2013) did find a weak but significant weakening of TTT intensity during MJO phase #1, and an enhancement during phase #6. Yet, how the association of different MJO phases and synoptic-scale convective regimes modulate the numbers and the daily intensity of extreme events, remains to be shown. Thus, in this study, we attempt to assess such combined influence on a newly developed typology of rainfall extreme (Ullah et al., 2022; Part I hereafter). Due to the rapidly changing patterns of these synoptic-scale convective regimes and intraseasonal variability related to MJO, these timescales are referred to as subseasonal timescales in the following sections.

In Part I, a novel typology of extreme rainfall events was proposed for NDJF season based on their spatial fraction as a base criterion, disentangling rainfall events into large-scale (Spatial fraction $\geq 7\%$) and small-scale extremes (spatial fraction $< 7\%$). The spatial fraction of an extreme event was defined as the proportion of South African rain-gauge stations or grid-points that simultaneously exceed their local 90th percentile threshold, regardless of their location, on the day of the event. These thresholds were found to be a good compromise to categorize extreme events according to their spatial extension. Intrinsic properties of both types of events were then explicitly assessed in the context of intraseasonal descriptors of rainfall variability (ISDs), characterizing the duration, spatial extension, and intensity of wet spells. NDJF total rainfall was found to be primarily shaped by large-scale extremes, which constitute, despite their rareness, more than half of the rainfall amount according to observation, and nearly half of it in ERA5. Observation (ERA5) shows an average of 8 ± 5 (20 ± 7) days per season associated with large-scale extremes, which are composed of 5 ± 3 (10 ± 3) spells with an average persistence of at least 2 days.

Here, we aim to investigate the variability of large- and small-scale extremes during NDJF at both (1) low-frequency (interannual and quasi-decadal) and (2) subseasonal (synoptic-scale and intraseasonal) timescales of variability. Such analyses are required to better identify the drivers of rainfall extremes in the region, to eventually promote multiyear seamless forecasts of extremes on one hand and improve subseasonal operational forecasts on the other hand.

This paper is organized as follows. Section 2 presents the data and methods. Section 3 investigates the influence of variability at low-frequency (interannual and quasi-decadal) timescales on rainfall extremes. Section 4 is dedicated to investigating the influence of variability at subseasonal (synoptic-scale and intraseasonal) timescales on rainfall extremes. The results are then summarized and discussed in section 5.

2 | DATA AND METHODOLOGY

2.1 | Investigating the variability of extremes at low-frequency timescales

To investigate the variability of extremes during NDJF at low-frequency timescales, the time series of two extreme ISDs, that is, wet days (WD_{EXT}) and total rainfall (TR_{EXT}) associated with large- and small-scale extremes are obtained from Part I. WD_{EXT} (TR_{EXT}) is defined as the average number of wet days (total rainfall amount)

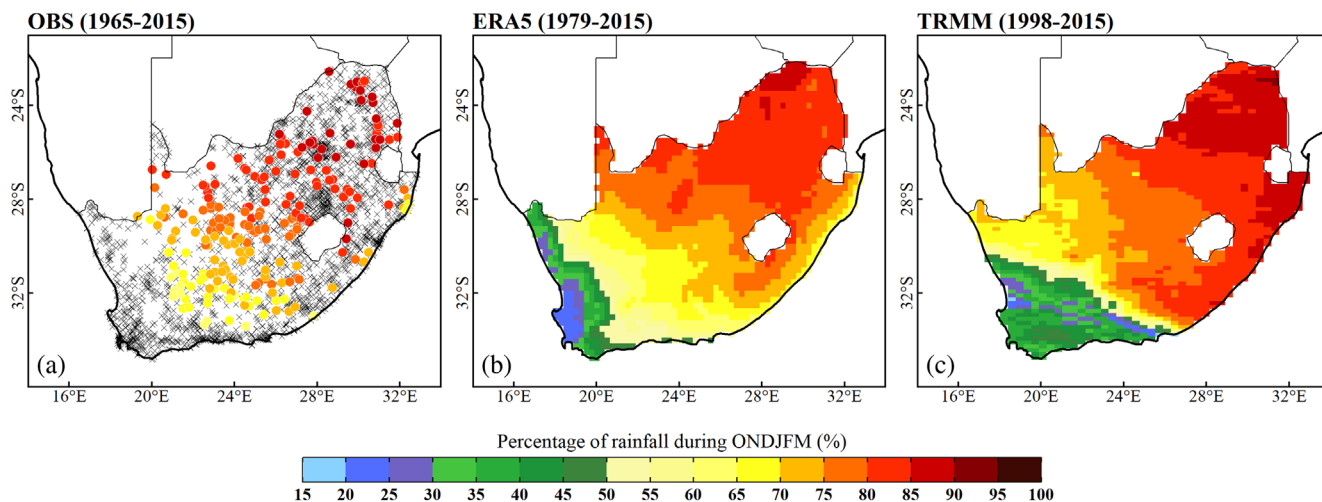


FIGURE 1 Spatial distribution of the percentage of rainfall during ONDJFM for OBS (a) for ERA5 (b) and for TRMM (c). The unqualified stations in (a) are indicated by black “x” symbols based on the seasonality test and/or other quality control measures [Colour figure can be viewed at wileyonlinelibrary.com]

associated with large- and small-scale extreme events in a season. These descriptors are computed using daily rainfall fields from the observational network of 225 stations (OBS) and deterministic members of ERA5 at a 0.25×0.25 global resolution over the period of 1975–2015. The choice of two extreme ISDs, that is, wet days and total rainfall is made because of the strong dependence of total rainfall in NDJF on the number of wet days associated with large-scale extremes, suggesting their key role in shaping total rainfall variability.

To account for the timescale dependence of teleconnections, we use the Summer Rainfall Index (SRI), as introduced by Dieppoos et al. (2016) using the Climatic Research Unit (CRU TS 3.23) and the Global Precipitation Climatology Centre reanalysis version 7.0 (GPCC.v7). SRI is here decomposed into two significant timescales of variability using a fast Fourier transform: 2–8 years interannual variability (IV) and 8–13 years quasi-decadal variability (QDV). The filtered SRI is linked to distinct modes of Pacific variability, namely the ENSO for IV and Interdecadal Pacific Oscillation (IPO) for QDV.

Monthly SST fields from the Extended Reconstructed Sea Surface Temperature, version 5 (Huang et al., 2017) of the National Climatic Data Centre are used for describing the large-scale climate background conditions modulating South African rainfall extremes and analysing teleconnections. This gridded data set is generated using in situ data from the International Comprehensive Ocean–Atmosphere Data Set release 3.0. In this release, several improvements are made, notably in quality control, bias adjustment and interpolation techniques, allowing for optimal reconstruction of sparse data over a 2×2 resolution grid (Huang et al., 2017). In addition, a

Niño3.4 index is calculated over the region of east-central equatorial Pacific between 5 N and 5 S, 170 W and 120 W, to monitor the state of ENSO and compute partial correlations of global SSTs, after linearly removing ENSO influence.

2.2 | Investigating the variability of extremes at subseasonal timescales

Observed daily rainfall data (OBS) from the Water Research Commission of South Africa (<http://www.wrc.org.za>; Figure 1a) is used for 225 stations spanning 50 years (1965–2015). As in Part I, these 225 stations are selected based on two conditions: (1) stations with less than 1% of missing values; (2) seasonality test, that is, stations for which 50% or more of the annual rainfall occurs during the austral summer season (Crétat et al., 2012).

ERA5 reanalysis Copernicus Climate Change Service (Hersbach et al., 2020) is the 5th generation reanalysis available from the European Centre for Medium-Range Weather Forecasts (ECMWF). Here we use the daily rainfall field for the 1979–2015 period, taken from the deterministic member at 0.25×0.25 global resolution (Figure 1b). Other variables used to assess the physical processes concerning statistical quantifications of extremes include vertically integrated moisture divergence (VIMD) and low-tropospheric moisture fluxes, which are derived from specific humidity, u -wind and v -wind at 850 hPa. Daily outgoing longwave radiation (OLR) fields are also obtained from the ERA5 ensemble to redefine the recurrent synoptic-scale convective regimes, following the methodology of Fauchereau et al. (2009).

Tropical Rainfall Measuring Mission (TRMM v.7) 3B42 product (Huffman et al., 2007) is used for satellite-based estimation of extreme rainfall events. TRMM precipitation product covers an area from 50 S–50 N and 180 W–180 E, with a spatial resolution of 0.25×0.25 , from 1998 to the present on a 3-hourly basis. The daily accumulated precipitation (combined microwave and infrared) is used here from 1998 to 2015 (Figure 1c). This dataset allows for a gridded estimation of rainfall, and corresponding extreme spells, thereby forming a useful complement to rain-gauges and reanalysis.

The MJO signal was extracted using two daily indices of the Real-time Multivariate MJO (RMM) index (Wheeler & Hendon, 2004), which uses 850 and 200 hPa zonal winds from NCEP/NCAR reanalysis (Kalnay et al., 1996) in addition to OLR daily fields.

2.3 | Examining the relationship between rainfall extremes and low-frequency timescales of variability

We first compute Pearson's correlation between global SST anomalies and the number of wet days and total rainfall associated with large- and small-scale extremes (cf., section 3.1). The analysis is then followed by an assessment of the timescale dependence of the teleconnections at the interannual and quasi-decadal timescales (cf., section 3.2).

The behaviour of rainfall extremes during different phases of IV and QDV is quantified using the Risk Ratio (RR) metric, commonly used in climate attribution studies (Paciorek et al., 2018). RR is defined as the ratio of the probability of an ISD under a factual scenario (P_F), to that probability under a counterfactual scenario (P_{CF}). Here, P_F (P_{CF}) corresponds to a period when a specific timescale of variability (i.e., SRI at IV or QDV timescale) is in the positive (negative) phase of the anomaly, and is given by

$$RR = \frac{P_F}{P_{CF}} = \frac{\left[\frac{a}{(a+b)} \right]_{IV|QDV}}{\left[\frac{x}{(x+y)} \right]_{IV|QDV}}, \quad (1)$$

where a (b) is the sum of a given ISD (i.e., number of wet days) when it lies in its positive (negative) phase of anomaly, when IV or QDV is in a positive phase, representing the P_F scenario. Similarly, x (y) is the sum of a given ISD (i.e., number of wet days) when it lies in its positive (negative) phase of anomaly, when the IV or QDV is in the negative phase, representing the P_{CF}

scenario. In addition, we also consider two thresholds obtained by using standard deviations (SD) of SRI at IV and QDV timescales to better quantify the behaviour of extreme ISDs: (1) the RR of extreme events in the weaker positive phase of SRI (P_F : IV or QDV > 0 and $< +0.5$ SD), as calculated concerning the weaker negative phase of SRI (P_{CF} : IV or QDV > -0.5 SD and < 0); (2) the risk of occurrence of extreme events in the strongly positive phase of SRI (P_F : IV or QDV $> +0.5$ SD), calculated concerning the strong negative phase of SRI (P_{CF} : IV or QDV < -0.5 SD). Physical mechanisms responsible for these changes in the RR metrics are assessed through composite anomalies of vertically integrated moisture divergence (VIMD) and moisture fluxes in each P_F and P_{CF} scenarios (cf., section 3.3).

2.4 | Examining the relationship between extremes and subseasonal timescales of climate variability

2.4.1 | Seasonality and network-density tests

Rainfall fields from OBS, ERA5 and TRMM are first submitted to the seasonality test. Hence, only the grid-points or stations for which 50% or more of the annual rainfall occurs during the austral summer season are retained (Figure 1a–c). Comparison with OBS may be biased by the weaker density and anisotropy of the rain-gauge network. Similarly, one can question whether the OBS network is dense enough to detect all extreme events, and more particularly small-scale events. To address these questions, for gridded ERA5 and TRMM fields, we alternatively consider all-grid-points (AGP), or only those nearest to OBS (NN). The NN and AGP fields of ERA5 (TRMM) have been named ERA5-NN and ERA5-AGP (TRMM-NN and TRMM-AGP), respectively. For conciseness, the results related to the NN fields of ERA5 and TRMM are shown in Supporting Information.

2.4.2 | Defining three types of rainfall extremes based on duration and spatial extension

To investigate the variability of extremes at subseasonal timescales, we focus on the day-to-day variability of large- and small-scale extremes in NDJF. We thus first identify the days associated with large- and small-scale extremes using the daily values of spatial fraction (i.e., the number of stations or grid-points exceeds simultaneously the local 90th percentile) and

complement this typology by introducing information related to the duration of the extreme rainy events. This allows us to differentiate between long-lived and short-lived large-scale extreme events. The local rainfall threshold is obtained as the 90th percentile for each station or grid-point. It is computed based on a normal distribution, and we note that it does not significantly differ from Gumbel and Gamma distribution (cf., Figure S1, Supporting Information), thereby suggesting statistical robustness in the definition of the local rainfall thresholds.

Including duration in the definition of extreme events is important since synoptic and intraseasonal ranges of variability play a major role in shaping the persistence of extreme events. On the one hand, the average spatial fraction defines the spatial scale or extent of the event and acts as a key to separate large-scale and small-scale extreme rainfall spells (Part I). On the other hand, their persistence acts as a parameter to distinguish between long-lived and short-lived events. Such characterization of rainfall extremes is not only novel for the region, but also essential to better understand the behaviour of rainfall extremes and their impacts, first in observations over recent years, and then under changing climate.

Large-scale long-lived events form a category of rainfall extremes that may potentially lead to high environmental and societal impacts. To date, the literature offers no clear statistical definition of such spells for the region. Part I depicts an average persistence of large-scale extreme events of 2 ± 1 days in observations. Based on the actual largest persistence values found over the study period and considering twice higher standard deviation, we retained a minimum threshold of at least 5 days as the best compromise to identify large-scale long-lived events. The definition of large-scale long-lived events should be used with caution since: (1) such spells are not defined based on their consequences on the environment and societies, but from an atmospheric point of view, considering the characteristics of the rainfall field itself; (2) we hypothesize that an event with larger spatial extension and longer persistence, therefore bringing huge amounts of water, is more likely to have major consequences for the regional water budget than other types of rainfall events.

Large-scale short-lived events are the counterpart of the previous type, but with a persistence of fewer than 5 days. Collectively, large-scale extreme rainfall events, regrouping short-lived and long-lived types, are important for the regional water balance since such events contribute to more than half of the total rainfall in the austral summer (Part I). The remaining

type of rainfall extremes corresponds to small-scale events, whose contribution to the total rainfall budget is much weaker (Part I). The persistence of these localized extremes may not provide a meaningful metric because they are more rarely embedded in large-scale circulation patterns likely to last more than a few hours/days. Thus, we consider small-scale extremes as a single category.

Overall, the different types considered in this work may be summarized as follows:

Large-scale long-lived events

Spatial fraction $\geq 7\%$ and *persistence* ≥ 5 days

Large-scale short-lived events

Spatial fraction $\geq 7\%$ and *persistence* < 5 days

Small-scale events

Spatial fraction $< 7\%$

2.4.3 | Characterizing the relationship between rainfall extremes and synoptic-scale variability

We first recalculate and update the work of Fauchereau et al. (2009) by applying the *k*-means algorithm on the latest available daily OLR fields from 10 ensemble members of ERA5 reanalysis between 1979 and 2015. OLR regimes are used as archetypes of the synoptic-scale convective variability over the region in NDJF. Figure S2 displays seven robust convective regimes based on ERA5 for NDJF, affecting southern Africa (Fauchereau et al., 2009). Three regimes (#5, #6 and #7) correspond to the typical signatures of TTT systems. Regime #5 refers to continental TTTs, which bring heavy convective rainfall over South Africa, while regimes #6 and #7 are shifted northeastwards, thereby bringing rainfall over the Mozambique Channel, Madagascar, and the southwest Indian Ocean (Macron et al., 2014, 2016; Pohl et al., 2018). Regimes #3 and #4 are generally associated with enhanced subtropical and extratropical convection, respectively, while regimes #1 and #2 refer to the drier conditions over South Africa (Figure S2). OLR anomalies shown here tend to be of larger magnitude than in Fauchereau et al. (2009), possibly due to a higher time sampling of the diurnal cycle of atmospheric convection in ERA5, and/or a much-increased spatial resolution compared to NOAA's satellite estimates. By applying the methodology proposed by Fauchereau et al. (2009) on the OLR fields from 10 ensemble members of ERA5, the regime for each day of NDJF season from 1979 to 2015 is identified and used for the comparative analysis with large- and small-scale extremes in this study (cf., section 4.1).

2.4.4 | Characterizing the relationship between rainfall extremes and intraseasonal variability related to MJO

Large-scale atmospheric convective patterns associated with the eight phases of the MJO over southern Africa are first obtained (Figure S3). The strongest wet and dry anomalies over South Africa are found during MJO phases #6–7 and #2–3, respectively, while moderate anomalies occur during other phases thereby corroborating Macron et al. (2016) and Grimm (2019). In NDJF, convective clusters associated with the MJO develop at phase #1 over the tropical Indian Ocean. The convective activity strengthens and propagates eastwards (phases #2–4) and reaches the Maritime continent (phases #4–5), before shifting to the Pacific (#5–6), American, and eventually Atlantic sectors (phases #7–8–1). During these MJO phases, clear-sky conditions tend to prevail over equatorial Africa and the nearby Indian Ocean (Wheeler & Hendon, 2004) but in phase #8 this situation starts changing again (Grimm, 2019). Two daily indices of MJO (phase and amplitude) of the RMM index are used to compare with rainfall extremes in this study (cf., section 4.2).

2.4.5 | Characterizing the combined influence of synoptic and intraseasonal variability of MJO on rainfall extremes

The combined influence of synoptic and intraseasonal variability on rainfall fields over southern Africa has already been studied (Hart et al., 2013; Macron et al., 2016; Pohl et al., 2009). Here, we attempt to investigate how synoptic and intraseasonal variability influence different types of extremes and can combine their respective influence. Potential changes in the occurrence and intensity of rainfall extremes during different OLR regimes and MJO phases are explored using contingency analysis by considering all possible combinations between OLR regimes and MJO phases (giving 56 different combinations; cf., section 4.3). To quantify potential dampening and/or enhancement in the intensity of extremes, we first compute the average of all 56 classes. The behaviour of each “class” is then presented in terms of anomaly against that mean value, and for each type of extreme (cf., section 4.3). Risk Ratio assessment is also used here to further explore the combined influence of MJO and synoptic-scale convective regimes on the number of large- and small-scale extremes and is given by

$$RR = \frac{P_F}{P_{CF}} = \frac{\left[\frac{a}{(a+b)} \right]_{\text{OLR regime and MJO phase of interest (MJO > 1.0 RMM)}}}{\left[\frac{x}{(x+y)} \right]_{\text{OLR regime and MJO phase of interest (MJO < 1.0 RMM)}}, \quad (2)$$

where a (b) is the sum of extreme (nonextreme) days when $\text{MJO} > 1.0$ RMM, representing the P_F scenario. Similarly, the x (y) is the sum of extreme (non-extreme) days when $\text{MJO} < 1.0$ RMM, representing the P_{CF} scenario. Following section 2.3, the composite anomalies of VIMD and moisture fluxes in each P_F and P_{CF} scenarios is also provided (cf., section 4.4).

3 | RAINFALL EXTREMES AT LOW-FREQUENCY TIMESCALES VARIABILITY

3.1 | Teleconnections of extremes with global SSTs

We first analyse the seasonal rainfall amounts due to daily extremes, and their contribution to seasonal rainfall totals. For each austral summer season between 1979 and 2015, Figure 2 presents the respective contribution of small-scale and large-scale extremes to total rainfall, as a function of the seasonal amounts. Rainfall extremes are responsible for a larger proportion of total rainfall when the austral summer rainfall amounts are low. This negative relationship is significant at 95% for both large-scale and small-scale extremes, and according to OBS and ERA5 reanalysis (Figures 2a,b and S4a). It denotes a weaker interannual variability of the rainfall amounts due to daily extremes than those caused by non-extreme rainy days. These same time series are also represented as a function of the seasonal mean Niño3.4 index during the same austral summer seasons (Figures 2c,d and S4b). The negative relationship between total austral summer rainfall and Niño3.4 is confirmed and is here extended to the seasonal amounts resulting from both small-scale and large-scale extremes. However, the ENSO dependency of the latter appears weaker than seasonal amounts. In the following, we further explore the driving mechanisms responsible for such changes, from 1 year or group of years to another, in seasonal extreme occurrence, and corresponding rainfall amounts.

Correlations between global SST fields and the seasonal occurrence of large- and small-scale extremes in NDJF are shown in Figure 3a, and the correlations between global SST fields and total rainfall associated with large-scale, small-scale and non-extreme rainfall

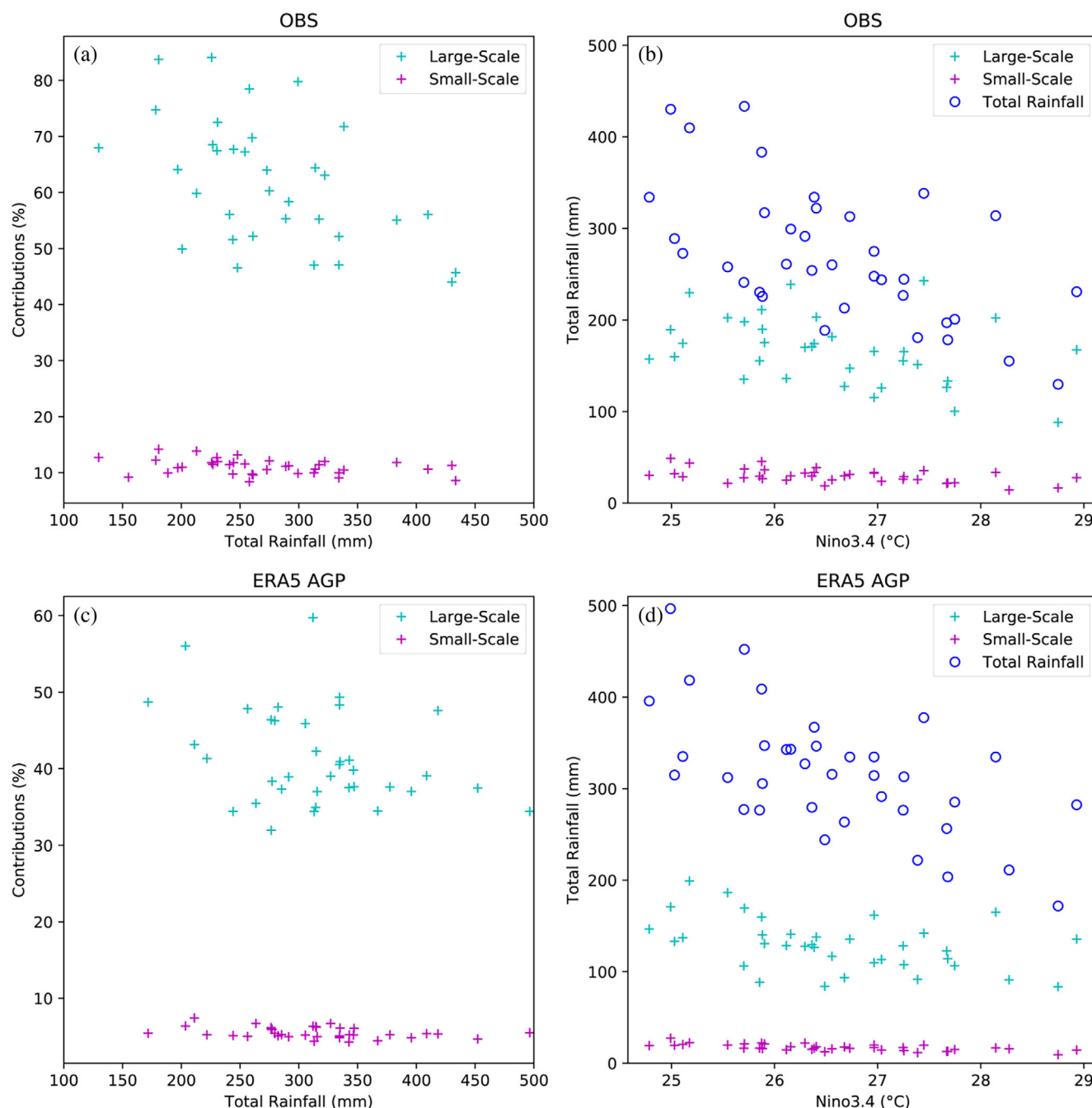


FIGURE 2 The contribution of large- and small-scale extremes (in percentage) to total rainfall during NDJF for OBS (a) and for ERA5-AGP (b). Seasonal total rainfall, total rainfall associated with large- and small-scale extremes as a function of Niño3.4 index is presented in (c) and (d) for OBS and ERA5-AGP, respectively [Colour figure can be viewed at [wileyonlinelibrary.com](https://onlinelibrary.wiley.com/doi/10.1002/joc.8059)]

totals are in Figure 4a. The contributions of these different rainfall types (in terms of percentage) to seasonal rainfall totals are also assessed with global SSTs (Figure 4b). To better identify potential sources of variability in the Atlantic, Southern and Indian Oceans, always strongly cross-correlated to ENSO these analyses have all been replicated after removing linearly the influence of ENSO (Figures 3b and 4c,d).

La Niña conditions have been identified in many previous studies as favourable to anomalously wet rainy seasons in southern Africa in austral summer. Figure 3a shows that they also favour the occurrence of large- and small-scale extreme events. Moreover, a warmer north Atlantic Ocean and west tropical Atlantic significantly favour the occurrence of extremes, especially large-scale ones (Figure 3a,b). Similarly, a colder Indian Ocean,

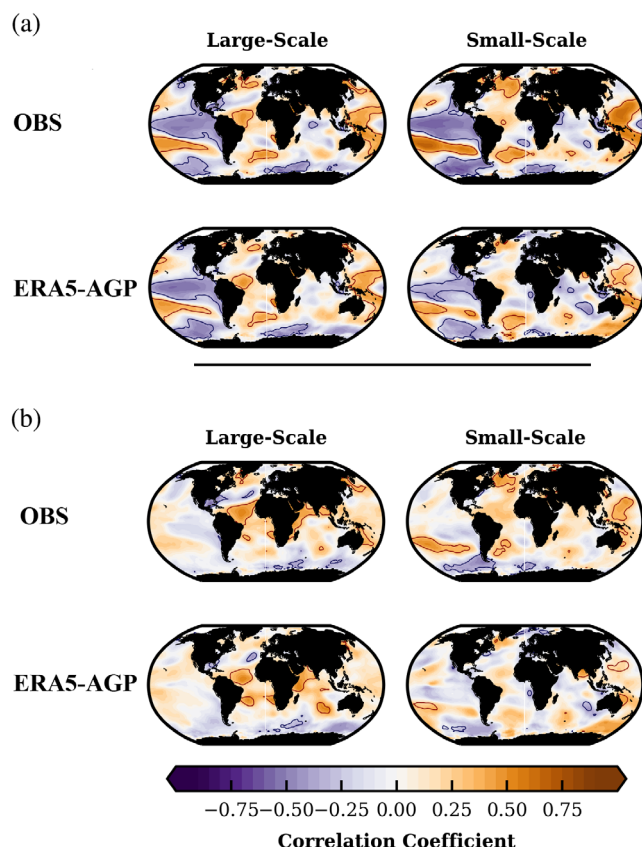


FIGURE 3 The correlation to global SST fields with the number of large- and small-scale extremes in the austral summer over the period of 1979–2015. The set of four panels in (a) refers to the correlation to global SSTs with the number of large-scale extremes (left panels) and for small-scale extremes (right panels) for OBS and ERA5-AGP. The same figure distribution is applied in (b), but the correlations are computed after removing the influence of ENSO. Niño3.4 index is used to compute partial correlations of global SSTs. Regions with solid contours indicate the correlations are significant at the 95% confidence level according to a Student's *t* test [Colour figure can be viewed at wileyonlinelibrary.com]

tropical east Atlantic Ocean and subtropical south Atlantic Ocean seem to favour the occurrence of small-scale extremes (Figure 3a). After linearly removing the influence of ENSO, we note that the correlation between large-scale extremes and SSTs in the north tropical Atlantic and subtropical south Atlantic is higher (Figure 3b). Interestingly, large-scale extremes are more strongly related to warmer SSTs in the north-west Indian Ocean, after removing the ENSO influence (Figure 3b), as observed during the anomalously wet summer following the 1997/1998 El Niño event (Lyon & Mason, 2007).

After removing ENSO influence, teleconnections with small-scale extremes become weaker (Figure 3b). ERA5 data suggest a significant relationship with the

subtropical Indian Ocean dipole (Dieppoiss et al., 2016, 2019; Pohl et al., 2018; Reason, 2001; Washington & Preston, 2006), but these results are not confirmed by OBS. By contrast, our results suggest that the variations in SSTs over the tropical southeast Atlantic mainly affect small-scale extremes in South Africa. Interestingly, organized correlation patterns of SSTs for large- and small-scale extremes are remarkably consistent using OBS and ERA5. The potential role of the tropical southeast Atlantic and associated Angola Current has been notably documented in previous studies (Desbiolles et al., 2020; Grimm & Reason, 2011; Rouault et al., 2003).

Figure 4 displays the correlation between global SSTs and total rainfall fields. Here, once again, La Niña conditions appear to favour wet conditions, including rainfall totals associated with large- and small-scale extremes, and non-extreme rainfall over South Africa. These results are consistent in all datasets (Figure 4a), confirming the results of Figure 2. Warmer conditions over the north Atlantic and west tropical Atlantic are also linked to rainfall caused by large- and small-scale extremes, especially in OBS (left and middle column panels in Figure 4a). Warm SST anomalies around the southern tip of the African continent (southeast Atlantic and southwest Indian Oceans) and cold SST anomalies in the Southern Ocean also tend to relate to total rainfall associated with large- and small-scale extremes (left and middle column panels in Figure 4a). However, these correlations are not significant with non-extreme rainfall (right column panel in Figure 4a). The latter appears better correlated with the south Atlantic Ocean and equatorial Indian Ocean (right column panel in Figure 4a), besides the equatorial central-east Pacific Ocean.

As illustrated in Figure 4b, the contribution of large- and small-scale extremes to total rainfall is positively correlated with the equatorial Pacific SSTs, suggesting that the contribution of extreme events to total rainfall is greater during El Niño and lower during La Niña. This may appear contradictory because drier conditions tend to prevail during El Niño (Crétat et al., 2012). Pohl et al. (2007) also suggested a larger influence of the MJO on South African rainfall during El Niño events, despite seasonal droughts. Here, this result is due to the stronger influence of ENSO on non-extreme days, while extreme-related rainfall is more constant interannually (Figure 2).

To better identify potential sources of variability in the Atlantic, Southern and Indian Oceans, this analysis is replicated after removing linearly the influence of ENSO on global SSTs (Figure 4c,d). When the ENSO influence is removed, correlations with the tropical Atlantic are stronger, for both large- and small-scale extremes (left and middle column panels in Figure 4c).

In OBS, the relationship between the eastern and tropical Indian Ocean and small-scale extremes also strengthens, but this is not the case for ERA5 (middle column panels in Figure 4c). The relationship between extreme conditions and SST anomalies in the Southern Ocean tend to weaken (Malherbe et al., 2016), which may be due to the interdependency between ENSO and the phase of the SAM in austral summer (Pohl et al., 2010). The influence of SIOD on large-scale extremes (left column panels in Figure 4d) is also clearer, in OBS, after removing ENSO influence, thereby suggesting a potential, yet secondary, influence on rainfall extremes in South Africa.

These results are consistent with previous studies that identified significant associations between southern African rainfall and SST changes in the Pacific (Dieppois et al., 2016, 2019), the southern Indian Ocean (Hoell & Cheng, 2018) and the Atlantic Ocean (Pomposi et al., 2018; Rapolaki et al., 2019, 2020). We complement these studies by assessing how these teleconnections also modify the occurrence of rainfall extremes, with a distinction made between small-scale and large-scale events as such analyses are meant to better identify their large-scale drivers.

3.2 | Timescale dependence of rainfall extremes

Figure 5 displays the linear correlation of the number of wet days and total rainfall associated with large- and small-scale extremes with the SRI filtered at interannual (IV) and quasi-decadal (QDV) timescales (Figure 5a,b), as in Pohl et al. (2018). A strong relationship between IV and the number of wet days associated with large-scale extremes is found using all datasets with a correlation between 0.70 and 0.72 (Figure 5a). The number of small-scale extremes seems weakly influenced at the IV timescale with correlations between 0.30 and 0.32 (Figure 5b). At the IV timescale, we note a consistent response of total rainfall associated with large- and small-scale extremes where all datasets show statistically significant correlations between 0.51 and 0.69 (Figure 5c,d). It is interesting to note that the number of small-scale extremes is weakly modulated at the IV timescale while the total rainfall at that timescale is strongly modulated. This could be due to the regional- to local-scale perturbations such as weaker TTTs and/or mesoscale convective complexes (MCCs) may have a larger influence on the number of small-scale extremes. In Part I, we note that small-scale

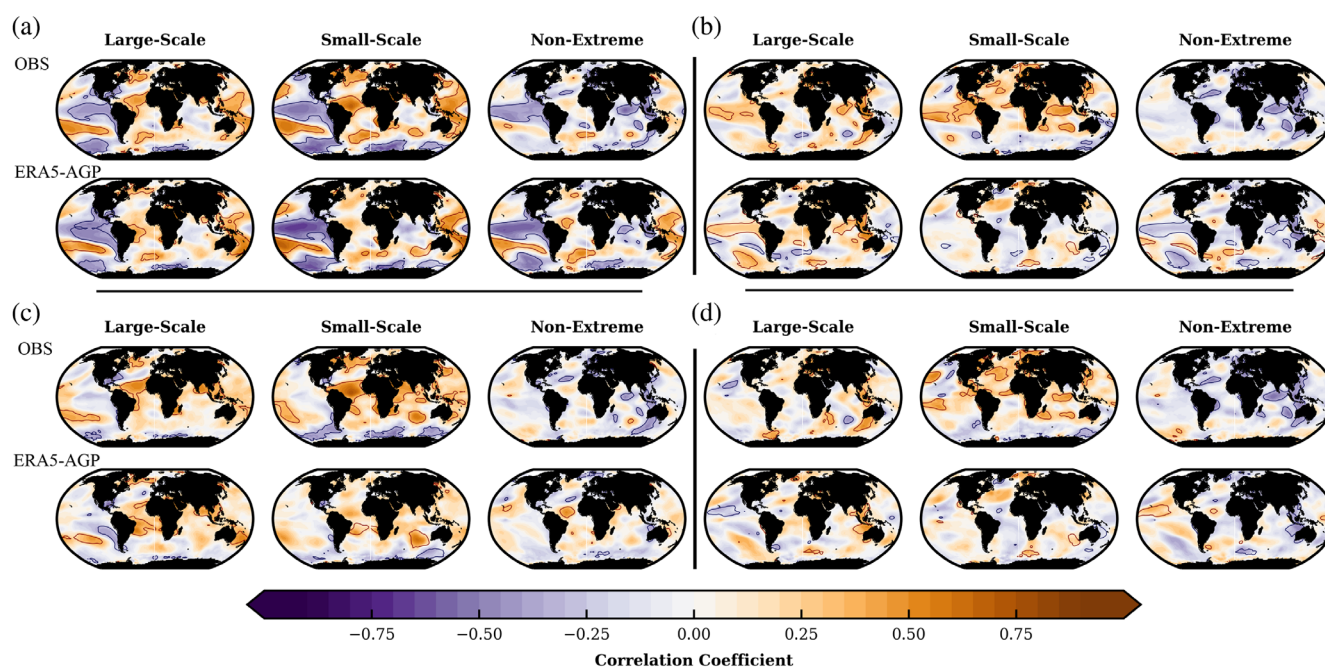


FIGURE 4 The correlation to global SST fields with total rainfall in the austral summer over the period of 1979–2015. The set of six panels in (a) refers to the correlation to global SSTs with total rainfall associated with large-scale extremes, small-scale extremes, and non-extreme rainfall (distributed column-wise from left to right, respectively) for OBS and ERA5-AGP. The set of six panels in (b) refers to the contributions of total rainfall associated with large-scale extremes, small-scale extremes, and non-extreme rainfall to total rainfall (distributed column-wise from left to right, respectively) for OBS and ERA5-AGP. The same figure distribution is applied in (c) and (d) but the correlations are computed after removing the influence of ENSO. Niño3.4 index is used to compute partial correlations of global SSTs. Regions with solid contours indicate the correlations are significant at the 95% confidence level according to a Student's *t* test [Colour figure can be viewed at [wileyonlinelibrary.com](https://onlinelibrary.wiley.com)]

extremes were largely embedded in non-extreme but spatially coherent rainfall events while extreme conditions were mostly located over the northeastern parts of South Africa (cf., Figures S4 and S5; Part I), a region known to be affected by MCCs (Blamey & Reason, 2013).

At the QDV timescale, all datasets show correlations between SRI and the number of both types of extremes of about 0.20 and 0.35 (Figure 5a,b). In contrast, the relationship of total rainfall associated with large-scale extremes is stronger at the QDV timescale, with correlations of about 0.48 and 0.50 (Figure 5c,d). However, the linear correlations at the QDV timescale are not significant according to the Bravais-Pearson test at $p = 0.05$ accounting for the autocorrelation in the time series. The latter dramatically decreases the actual number of degrees of freedom, thereby leading to a biased significance assessment.

3.3 | Risk assessment at low-frequency timescales

To better assess the potential variations in ISDs at IV and QDV timescales, we estimate these variations through changes in the risk ratio RR. Figure 6a displays the RR metric for the number of wet days associated with large- and small-scale extremes computed for the weaker positive phase (P_F : IV > 0 and IV < +0.5 SD) with respect to the weaker negative phase (P_{CF} : IV > -0.5 SD and IV < 0) of IV timescale using OBS and ERA5-AGP. For large-scale extremes, OBS and ERA5-AGP show RR of about 1.32 and 1.41, respectively, with a narrow bin of confidence interval between 1 and 2 (Figure 6a). This suggests that the number of large-scale extremes at the weaker positive phase of IV timescale could be 32%–41% higher as compared to the weaker negative phase of IV

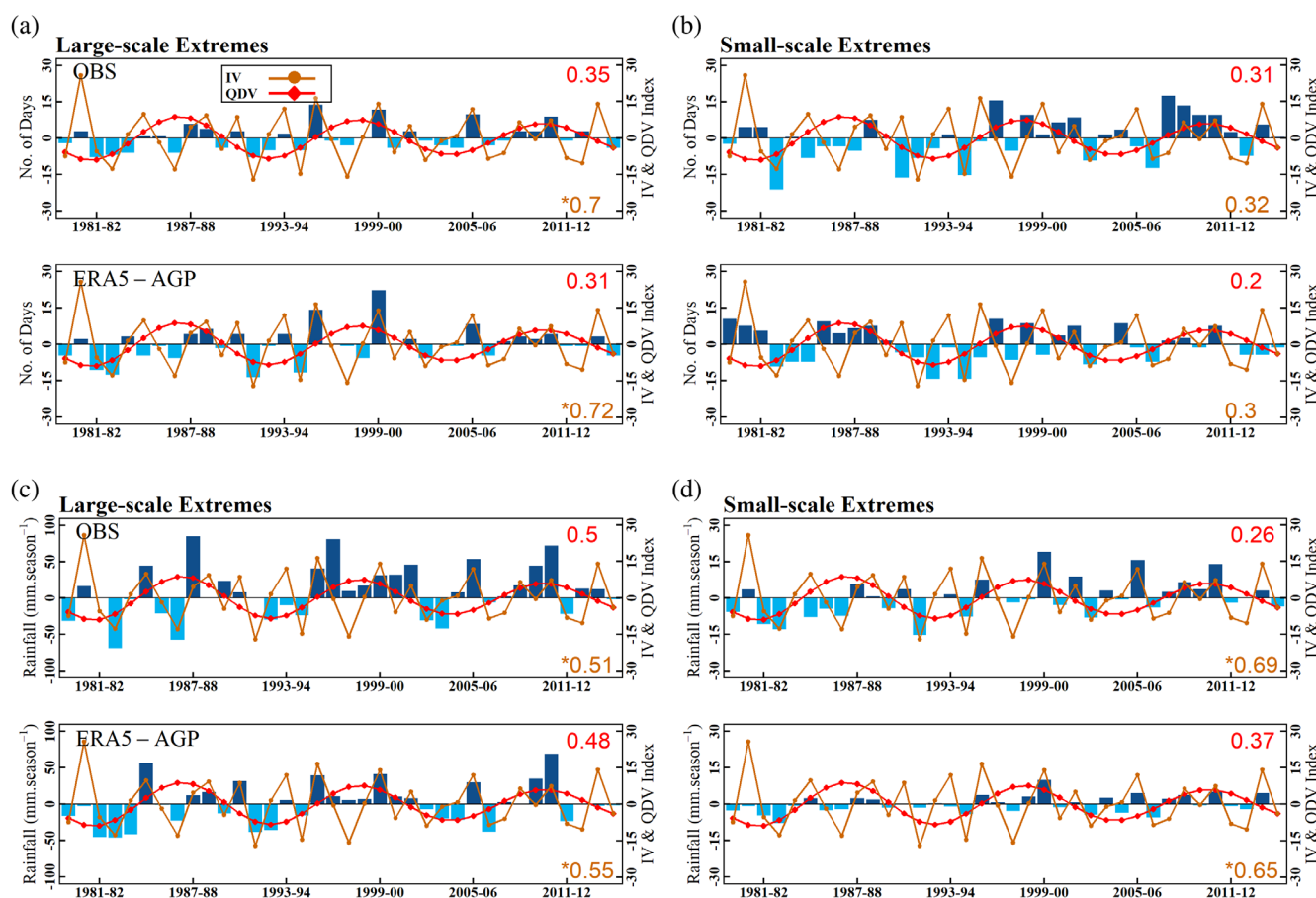


FIGURE 5 Anomalies of extremes ISDs (blue bars), SRI at the IV timescale (brown line) and SRI at the QDV timescale (red line) are presented in four panels for wet days associated with large-scale extremes (a) and small-scale extremes (b), distributed row-wise from top to bottom for OBS and ERA5-AGP, respectively. The same figure distribution is applied in (c) and (d) but the analysis is performed for total rainfall associated with large- and small-scale extremes. The correlation of each ISD with IV (QDV) is displayed at the bottom (top) of each panel using the same colour as used for their timeseries. The y-axis on left-hand-side in each panel is used to display the unit of ISDs while the y-axis on right-hand-side is commonly used for SRI corresponding to IV and QDV index. The correlations marked with “*” are significant at $p = 0.05$ according to the Bravais-Pearson test [Colour figure can be viewed at [wileyonlinelibrary.com](https://onlinelibrary.wiley.com)]

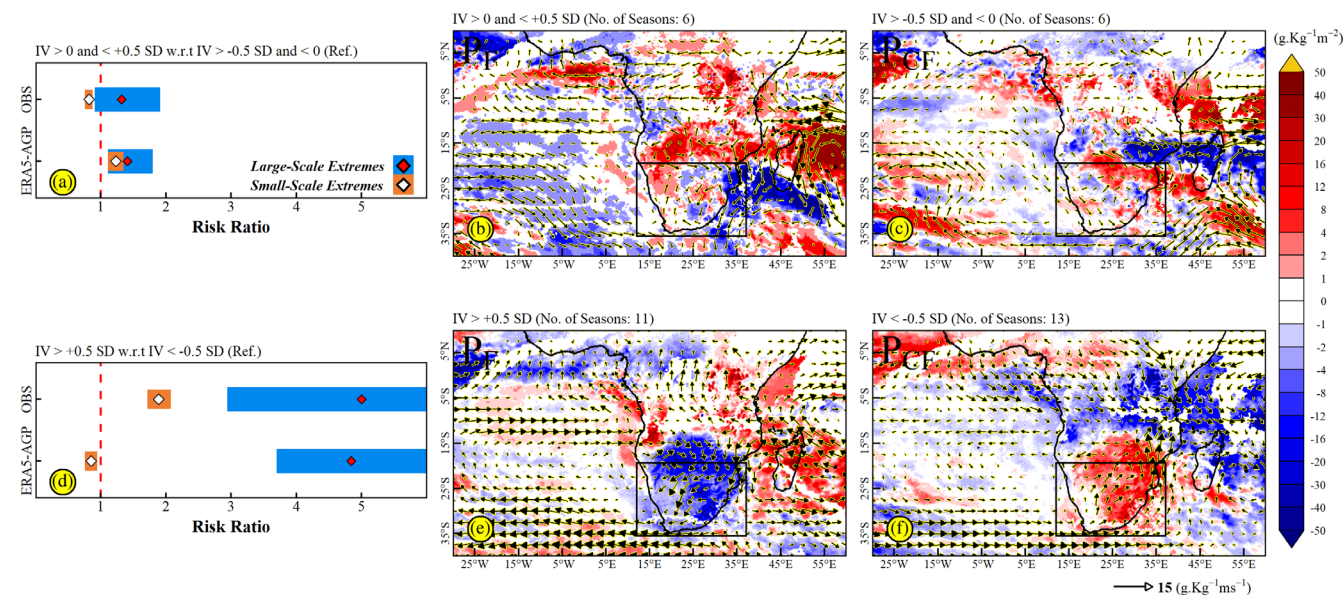


FIGURE 6 Estimated risk ratio computed for wet days associated with large- and small-scale extremes computed for the P_F scenario, i.e., the period when $IV > 0$ and $< +0.5$ SD (weaker positive phase of IV) with respect to P_{CF} scenario i.e., the period when $IV > -0.5$ SD and < 0 (weaker negative phase of IV) (a). The red (white) symbols represent the numerical position of risk ratio for large-scale extremes (small-scale extremes) computed at $p = 0.05$. The horizontal expansion of stripes (blue and brown for large- and small-scale extremes, respectively) represents the minimum and maximum limits of the 95% confidence interval. $RR = 1.0$ corresponds to an equiprobable risk of occurrence of extremes either in P_F scenario or in P_{CF} scenario. A risk ratio above or below 1.0 can be interpreted with a factor, for instance, 0.2, 0.4 and 0.6 indicate a 20%, 40% and 60% higher risk of occurrence of extremes during P_F scenario as compared to the P_{CF} scenario or vice versa if below 1.0. The composite anomalies of vertically integrated moisture flux divergence ($\text{g kg}^{-1} \text{m}^{-2}$) and moisture flux ($\text{g kg}^{-1} \text{ms}^{-1}$) at 850 hPa for both periods which are considered to compute the risk ratio are shown in (b) and (c) where only those anomalies are shown which are significant at 95% confidence level according to the one-tailed Student's t test. The panels are distributed similarly in the second row but here the risk ratio for large- and small-scale extremes is computed for the P_F scenario, that is, the period when $IV > +0.5$ SD (strong positive phase of IV) with respect to P_{CF} scenario, that is, the period when $IV < -0.5$ SD (strong negative phase of IV) (d–f) [Colour figure can be viewed at [wileyonlinelibrary.com](https://onlinelibrary.wiley.com/doi/10.1002/joc.8059)]

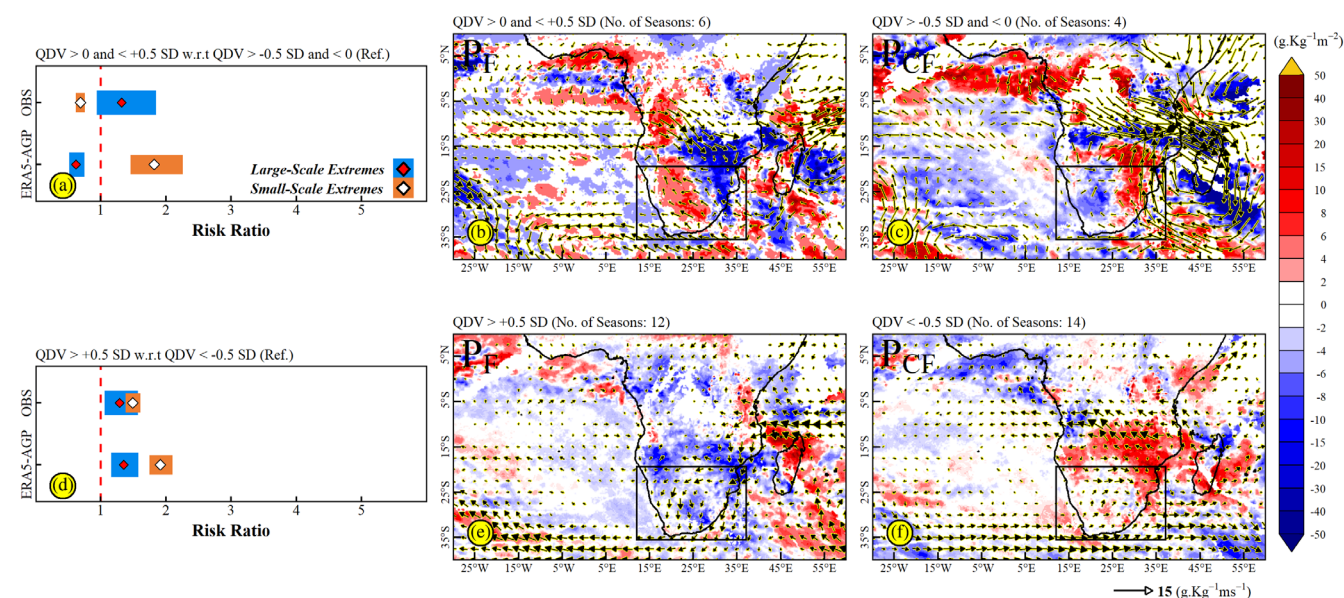


FIGURE 7 Same as Figure 6 but for QDV timescale [Colour figure can be viewed at [wileyonlinelibrary.com](https://onlinelibrary.wiley.com/doi/10.1002/joc.8059)]

Intraseasonal Calendar of daily rainfall extremes using OBS, ERA5-AGP and TRMM-AGP

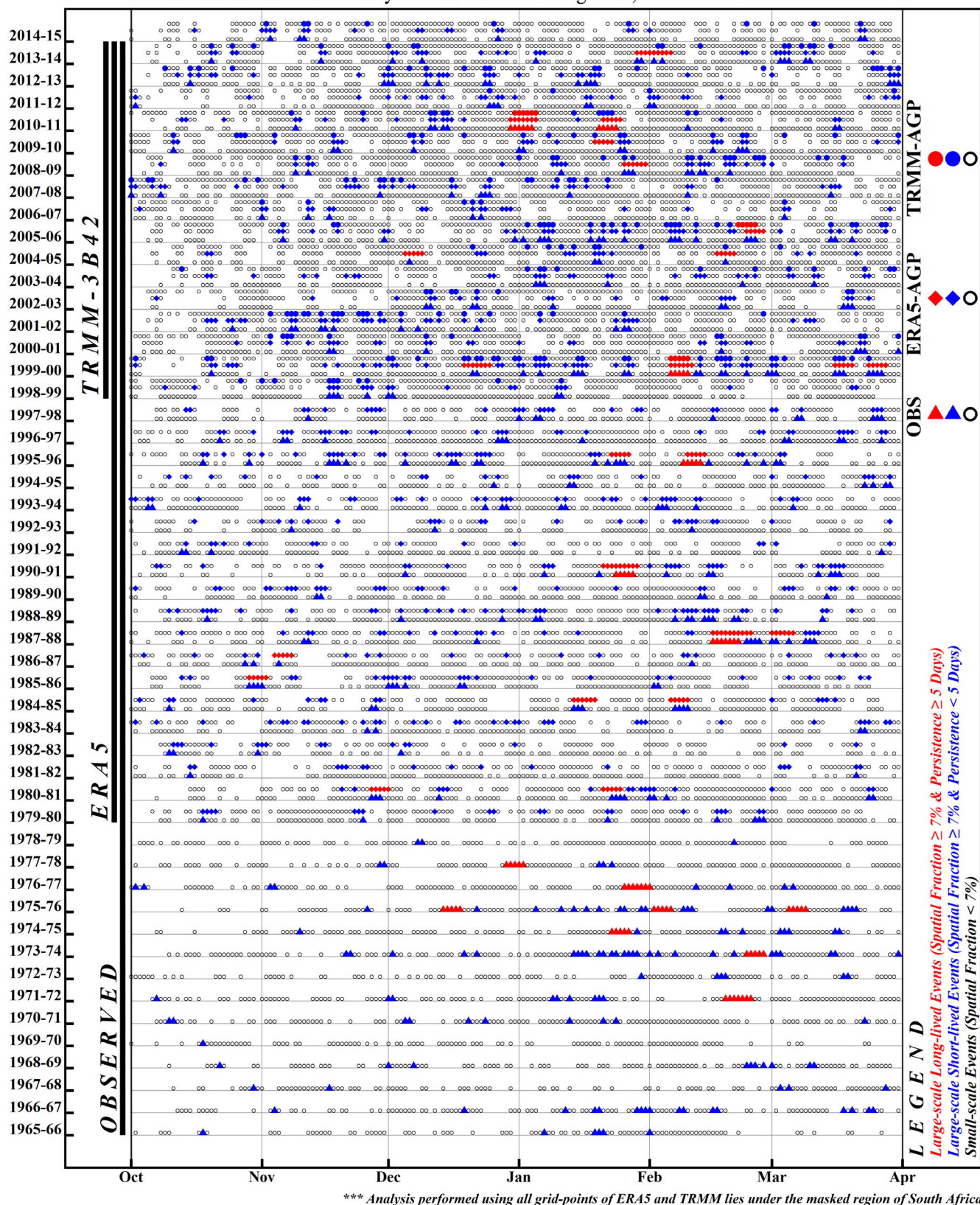


FIGURE 8 Legend on next page.

timescale. Figure 6b,c shows the composite anomalies of VIMD and moisture flux at 850 hPa corresponding to P_F and P_{CF} scenario, respectively. Weaker anomalies prevail during both scenarios yet during P_F scenario, slightly higher convergence over the northeastern and some central domains of South Africa are quite notable which are leading to a 32%–41% rise in the risk of occurrence of large-scale extremes as compared to P_{CF} scenario.

Figure 6d shows a similar analysis but RR is computed for the number of days associated with extreme events occurring during the stronger positive phase (P_F : IV > +0.5 SD) with respect to the number of days associated with the extreme events occurring during the stronger negative phase (P_{CF} : IV < −0.5 SD) of the IV timescale. OBS and ERA5-AGP indicate a RR of nearly 5 with a confidence interval of about 3–7 suggesting; (1) a 400% higher risk on the numbers of large-scale extreme wet days when IV lies in a strong positive phase, as compared to its stronger negative phase; (2) larger confidence interval suggests anomalously wet conditions with a higher number of large-scale extremes (Figure 6d). In OBS, small-scale extremes are more frequent during the P_F scenario of IV timescale with a RR of about 1.89 with a narrow bin of confidence interval suggesting that the number of such extremes is less variable (Figure 6d). Extended to Madagascar, wet and dry dipole conditions clearly prevail over 20°S during P_F and P_{CF} scenarios of IV timescale (Figure 6e,f). Figure 6e clearly represents the moisture flux convergence over South Africa during strong La Niña conditions. Another notable signal is the location of Angola low, which is known as a tropical source of convergent moisture that can next be embedded in TTTs (Reason & Jagadheesha, 2005). This could result in increased occurrence of large-scale extremes during the seasons when IV > +0.5 SD. Such moisture flux anomalies as shown in Figure 6e are also well discussed by Hoell and Cheng (2018) as they identified such anomalies because of La Niña and positive SIOD phasing. In such cases, cyclonic circulation prevails over southern Africa and anticyclonic circulations over Madagascar and the adjacent Indian Ocean. Nearly opposite features of VIMD and moisture fluxes appear during the composites of the seasons when IV < −0.5 SD. Here, strong divergent

anomalies represent departure of moisture from southern Africa thus enhancing dry conditions (Figure 6f).

Figure 7a displays the risk ratio assessment for the number of large- and small-scale extremes computed for the weaker positive phase (P_F : QDV > 0 and QDV < +0.5 SD) with respect to the weaker negative phase (P_{CF} : QDV > −0.5 SD and QDV < 0) of SRI at QDV timescale. OBS data show a RR of 1.32 with a confidence interval between 0.94 and 1.85, suggesting that the numbers of large-scale extremes are typically 32% higher in the P_F scenario of QDV timescale as compared to P_{CF} (Figure 7a). The convergence signals found over southern Africa during P_F scenario of QDV timescale may related to the moisture transport patterns associated with SICZ, which is formed by the convergence between the South Atlantic westerlies and the South Indian easterlies (Figure 7b). However, during P_{CF} scenario of the QDV timescale, we note a strong cyclonic circulation over Madagascar and southeast Indian Ocean, with moisture convergence over Madagascar and divergence from eastern parts of southern Africa (Figure 7c). Such anomalies indicate: (1) strong equatorial moisture anomalies over Indian Ocean and southernly anomalies over southern Africa; (2) strong influence of the Indian Ocean warming on low-level circulation and moisture, all together bringing dry conditions over the regions (at least for the large-scale extreme events).

No substantial change in the RR metric emerges in the number of large-scale extremes when QDV lies in its strong positive phase (P_F : QDV > +0.5 SD), with respect to its strong negative phase (P_{CF} : QDV < −0.5 SD; Figure 7d). However, OBS and ERA5-AGP show a RR of about 1.29–1.35 for large-scale extremes with a confidence interval varies in between 1.06 and 1.58, suggesting that such extremes could be 29%–35% higher, and can be increased by up to 58%, during P_F scenario of QDV timescale as compared to its P_{CF} scenario. For small-scale extremes, both datasets show a RR of about 1.49–1.91 with a confidence interval between 1.38 and 2.1 (Figure 7d). Notably, the RR for small-scale extremes is slightly higher as compared to the RR of large-scale extremes, this suggests that variability at the QDV timescale has a larger influence on

FIGURE 8 Intraseasonal calendar of extreme rainfall typology for OBS (1965–2015), ERA5-AGP (1979–2015), and TRMM-AGP (1998–2015) for the extended austral summer season ONDJFM. Large-scale long-lived (large-scale short-lived) rainfall spells for OBS, ERA5-AGP and TRMM-AGP are presented in red symbols “▲,” “◆” and “●” (blue symbols “▲,” “◆” and “●”), respectively. Small-scale events are displayed in black symbols “ ” regardless of the dataset. The shape of the symbol represents the dataset, and the colour represents the type of the event (i.e., large-scale long-lived or short-lived) which is based on the duration of the persistence of a spell. The intraseasonal calendar is produced for extended austral summer season (October–March) and distinct baseline periods depending on data availability (OBS: 1965–2015, ERA5: 1979–2015 and TRMM: 1998–2015). The extended season is selected here to investigate the occurrence of large-scale long-lived events during onset (October) and cessation (March) months of core rainy season [Colour figure can be viewed at wileyonlinelibrary.com]

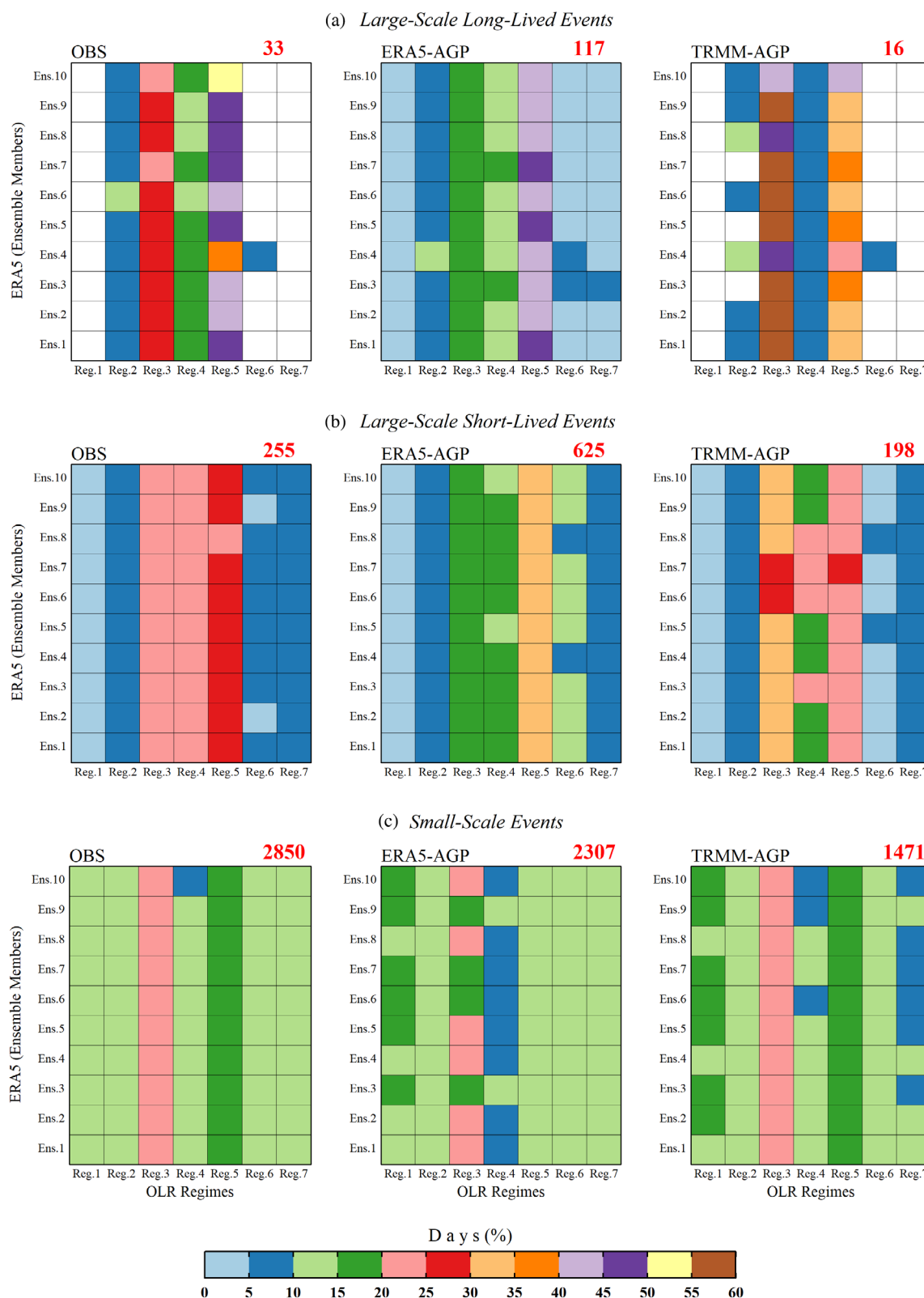


FIGURE 9 The co-occurrence of different types of rainfall extremes identified by OBS, ERA5 and TRMM during NDJF over the period of 1979–2015 in seven OLR regimes produced by 10 ensemble members of ERA5. Panels are distributed row-wise from top to bottom for the days associated with large-scale long-lived events (a), large-scale short-lived events (b) and small-scale events (c). The reference values are displayed at the upper-right corner of each panel in red letters (i.e., the total number of days of associated with respective type of extreme events identified by each dataset). Colour shading displays how these reference values are distributed in terms of percentage in seven OLR regimes produced by 10 ensemble members of ERA5 [Colour figure can be viewed at [wileyonlinelibrary.com](https://onlinelibrary.wiley.com/doi/10.1002/joc.8059)]

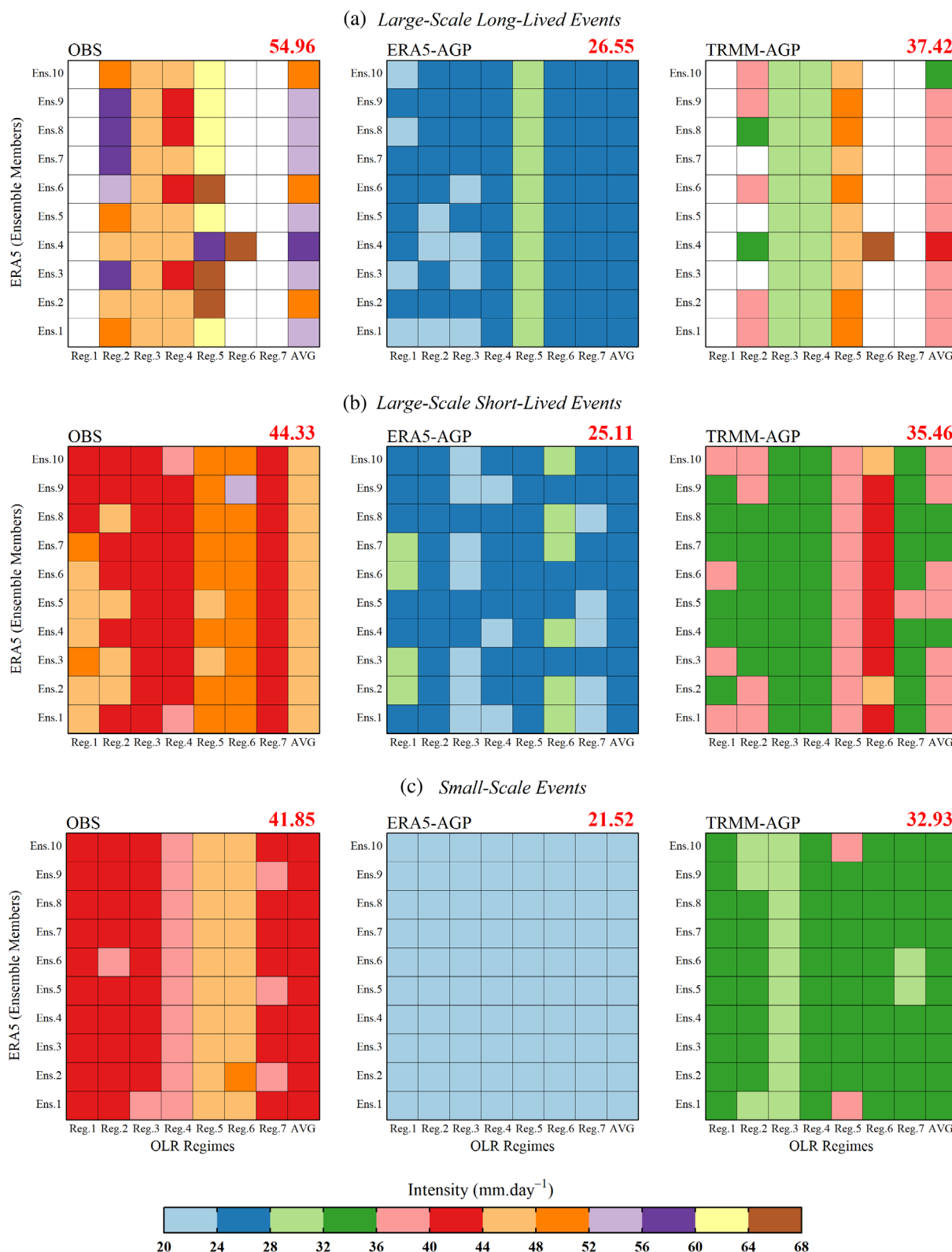


FIGURE 10 Same as Figure 9 but for intensity except the reference values are displayed at the upper-right corner of each panel in red letters are the average intensity of respective type of extreme events identified by each dataset [Colour figure can be viewed at [wileyonlinelibrary.com](https://onlinelibrary.wiley.com/doi/10.1002/joc.8059)]

the numbers of small-scale extremes (Figure 7d). The RR value is lesser in OBS for small-scale extremes as compared to ERA5-AGP suggesting: (1) a critical deficiency of

network density in OBS particularly for small-scale extremes; (2) the viability of using ERA5-AGP to deal with the network density issue in OBS.

Figure 7e,f displays the composite anomalies of VIMD and moisture flux for P_F and P_{CF} scenarios related to strong opposite phases of the QDV timescale. During P_F scenario, an easterly moisture flux from the South Indian Ocean is quite notable over tropical southern Africa (above 15 S), the moisture flux then propagates toward the southwestern regions before converging over the northeastern parts of South Africa (Figure 7e). Dieppois et al. (2016) suggest that the moisture fluxes from the Indian Ocean converge with southeasterly moisture fluxes from the South Atlantic High, thereby strengthening the SICZ and this relates to a northward shift of the Intertropical Convergence Zone (ITCZ), north of Madagascar from the western Indian Ocean to central Africa.

The results of RR for small-scale extremes shown by OBS and ERA5-AGP are in line with the previous section, where we note that the total rainfall associated with small-scale extremes is well correlated with the SRI at QDV timescale (cf., Figure 5c). Second, shallow convergence and weaker moisture flux over South Africa indicate why the risk of large-scale extremes is comparatively lesser than the risk of small-scale extremes.

In this section, we attempt to quantify changes in the occurrence of extreme events using the varying magnitude of SRI on IV and QDV timescales. The SRI is a rainfall index, selected over a homogeneous region and partially shaped by extremes itself. This suggests that the SRI and daily extremes are not independent of each other, due to the major contribution of large-scale extremes to rainfall totals (Part I). The quantifications

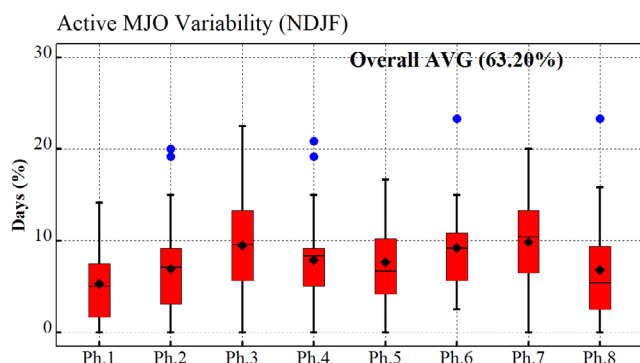


FIGURE 11 The box and whisker plots display the active MJO variability during NDJF from 1979 to 2015 computed by considering only those days in each phase where the amplitude exceeded 1.0 RMM index. The lower and upper end of red box show the lower and upper quartile, respectively, while the black line indicates the median of the distribution. The whiskers at the bottom and top indicate the lower and upper extreme of the distribution. The black “◆” and blue symbols “●” indicate mean and outliers of the distribution, respectively [Colour figure can be viewed at wileyonlinelibrary.com]

made using RR are in line with the physical mechanism shown via changes in the moisture fluxes and divergence. We note that the effect of the SRI at IV timescale on the RR is particularly stronger for the large-scale extremes. The analysis presented in section 3 is also provided for NN fields of ERA5 in Figures S4–S7.

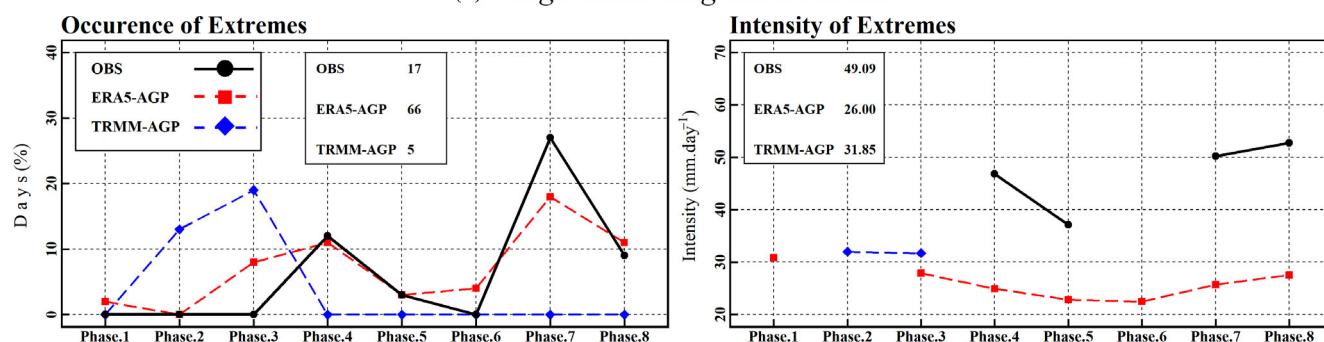
4 | RAINFALL EXTREMES AT SUBSEASONAL TIMESCALES

In this section, we attempt to quantify the changes in daily rainfall extremes at subseasonal (synoptic-scale and intraseasonal) timescales. To that end, we first complement the typology of rainfall extremes with duration statistics (section 2.4.2) prior to investigating the characteristics of extremes. Figure 8 shows an intraseasonal calendar of complemented typology of rainfall extremes. All days associated with large-scale long-lived events in OBS are also identified using the all-grid-points fields of ERA5 and TRMM. A similar analysis is then applied to the nearest neighbour fields of ERA5 and TRMM where both datasets generally show remarkable efficiency in monitoring large-scale long-lived extremes (Figure S8). This allows us to conclude that the density of the observational network (i.e., 225 stations) seems sufficient to detect most large-scale long-lived rainfall spells. Figure 8 also shows that the occurrence of large-scale long-lived extremes in the onset and cessation months of the austral summer is substantially fewer than during the core of the rainy season. No event is detected by OBS during October and only one in March of 1975/1976 summer, except a few spells detected by ERA5 and TRMM in March (Figures 8 and S8). A list of large-scale long-lived rainfall spells identified by OBS is provided in Table S1.

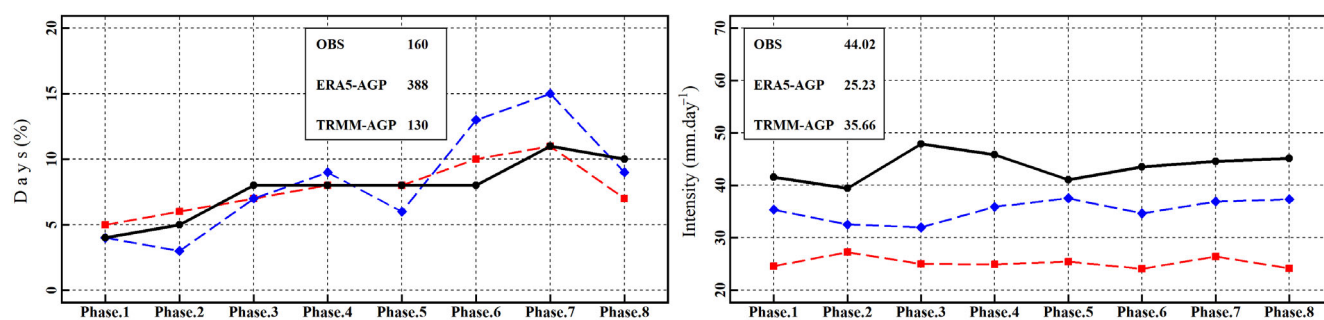
4.1 | Characteristics of rainfall extremes in synoptic-scale convective regimes

Figure 9 displays the co-occurrence of different types of rainfall extremes identified by OBS, ERA5 and TRMM in each synoptic-scale convective regime. About 45%–50% of days associated with large-scale long-lived events occur during regime #5, corresponding to the continental TTT events whereas about 20%–30% of these days occur during regimes #3 and #4, respectively (cf., Figure S2). The days associated with large-scale short-lived events, which are more frequent than large-scale long-lived ones, mostly occur during the same regimes (#3, #4 and #5: Figure 9b). These results are consistent in OBS, ERA5 and TRMM, albeit a slightly lower contribution for the two latter (Figure 9b). Small-scale extremes are more

(a) Large-Scale Long-Lived Events



(b) Large-Scale Short-Lived Events



(c) Small-Scale Events

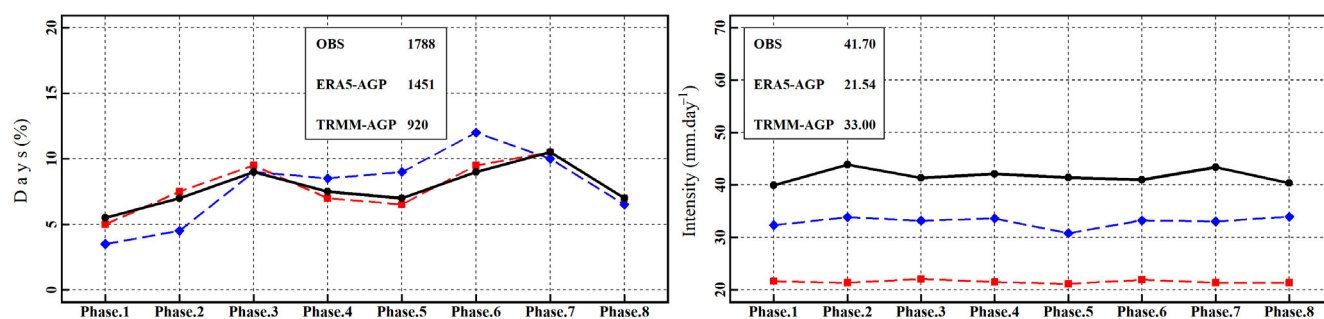


FIGURE 12 The occurrence and intensity of different types of rainfall extremes during NDJF in convective regimes associated with eight MJO phases during the period of 1979–2015. Panels on the left (right) refer to the occurrence (intensity) and are distributed row-wise from top to bottom for the days associated with large-scale long-lived events (a), large-scale short-lived events (b), and small-scale events (c). The reference values (i.e., the total number of days or average intensity of respective type of extreme events as identified by each dataset) are displayed inside each panel. The reference values are computed by considering only those days in each phase where the amplitude exceeded 1.0 RMM index of the MJO [Colour figure can be viewed at [wileyonlinelibrary.com](https://onlinelibrary.wiley.com)]

likely during regimes #3 and #5 with a contribution of 25% and 20%, respectively (Figure 9c). The days associated with large-scale events occur largely during synoptic regimes #3 to #5 describing the precursors and then the mature phases of continental TTT systems (Fauchereau et al., 2009). However, according to the lead-lag composites of circulation and convection anomalies associated with different bands of intraseasonal variability in southern African monsoon, presented by Silvério and Grimm (2022), the TTT pattern (here identified as the regime #5) is part of the evolution of these anomalies and is

preceded and followed by anomaly patterns like regimes #3 and #6.

Regarding the daily average intensity of each type of extreme event during different OLR regimes, we note that large-scale long-lived events appear slightly more intense during regime #5, with an average intensity exceeding 60 mm day^{-1} in OBS and TRMM (Figure 10a). This is consistent with previous studies (Hart et al., 2013; Macron et al., 2014), showing that TTTs produce heavier and more extreme rainfall than normal. In OBS, the overall average intensity of large-scale short-lived events is

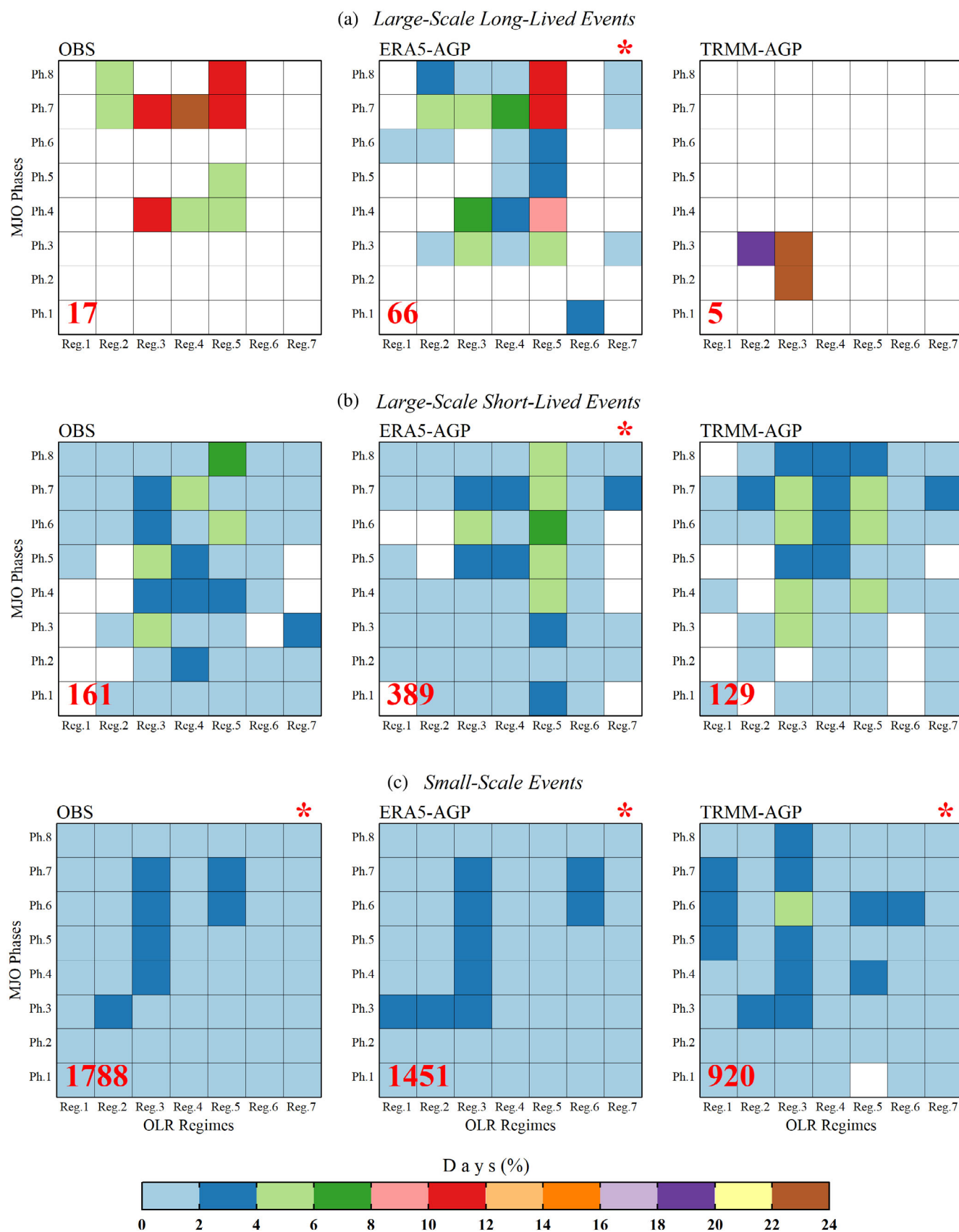


FIGURE 13 Legend on next page.

44.33 mm day⁻¹ but regime-to-regime differences are substantially larger (OBS panel in Figure 10b). Large-scale short-lived events tend to be 8%–23% more intense in regimes #5 and #6 even though they are less likely during regime #6 (Figure 10b). Such higher intensity during regimes #5 and #6 is also found in ERA5 and TRMM, but they underestimate the average intensity of large-scale short-lived events (Figure 10b).

Small-scale extremes also display slightly higher intensity during regimes #5 and #6 where OBS shows an average intensity of about 48 mm day⁻¹ as compared to 40–44 mm day⁻¹ during other regimes (Figure 10c). In ERA5, no remarkable differences appear in the intensity of small-scale events across different regimes and ensemble members (ERA5 panels in Figure 10c). Overall, intermember differences are lower for small-scale extremes, while, for other types of extremes, the behaviour of ensemble members is slightly more variable.

4.2 | Characteristics of rainfall extremes in different MJO phases

As illustrated in Figure 11, between 1979 and 2015, 63% of austral summer days are associated with active MJO variability (Amplitude >1). To assess the regional response of MJO phases on different types of rainfall extremes, we assess how the numbers of extremes, and their corresponding intensities, vary according to the MJO phases (Figure 12).

Around 9%–27% of days associated with large-scale long-lived events occur in MJO phases #7 and #8 as shown by OBS and ERA5-AGP, while in phase #4 these datasets indicate 11% to 12% of days associated with such events (left panel in Figure 12a). TRMM shows different results and yields higher numbers of days associated with large-scale long-lived events during MJO phases #2 and #3, questioning the robustness of this dataset (left panel in Figure 12a). Particularly in OBS, we note that days of large-scale long-lived events are more intense during MJO phases #7 and #8, with an average intensity exceeding 50 mm day⁻¹ (right panel in Figure 12a).

The number of wet days associated with large-scale short-lived extremes are higher in austral summer during MJO phases #6–8 (28%–37%), moderately frequent in phases #3–5 (21%–24%) and less frequent in phases #1–2 (7%–11%), and these results are consistent for all datasets (Figure 12b). The intensity of large-scale short-lived extremes appear slightly lower during phases #1–2, while an extremely high-intensity signal in OBS is notable during phases #3–8 with an average intensity of about 41.05–47.86 mm day⁻¹ (right panel in Figure 12b). Similar results emerge for the number of days associated with small-scale extreme events, where MJO phases #1–2, #3–5 and #6–8 show frequencies of about 8%–12.5%, 21.5%–26.5% and 26.5%–30.5%, respectively (left panel in Figure 12c). No remarkable inter-phase differences appear for the intensity of small-scale extreme events (right panel in Figure 12c). Overall, regardless of the type of extreme events, we note therefore that the numbers of extremes are lesser in MJO phase #1–2, moderate in #3–5 and higher in #6–8. These coherent and successive groups of MJO phases are referred to hereafter as dry, moderate, and wet MJO phases, in the context of South African rainfall extremes.

4.3 | Characteristics of rainfall extremes during the combined influence of synoptic-scale (OLR regimes) and intraseasonal variability (MJO)

We assess here the combined influence of synoptic-scale convective regimes and MJO phases on the different types of extremes. Contingency analysis is provided for the number of days associated with different types of extremes and their corresponding intensity in Figures 13 and 14, respectively.

In Figure 13a, OBS and ERA5 suggest that the days associated with large-scale long-lived events are largely occurring in regimes #3 to #5 during moderate and wet MJO phases. Large-scale short-lived events also exhibit few notable and robust associations: (1) regime #5 with phase #6 with a contribution of 6%–8% of days according

FIGURE 13 Concomitance between OLR regimes and MJO phases for number of days associated with different types of extremes during NDJF over the period 1979–2015, distributed row-wise for the days associated with large-scale long-lived events (a), large-scale short-lived events (b), and small-scale events (c). For 8 phases of the MJO, only those days are considered in which the MJO amplitude exceeded 1.0 RMM index. The panels indicated by “*” are significant according to the chi-square test at $p = 0.05$. The reference values are the total number of days of a respective type of extreme event identified by datasets and displayed at the bottom-left corner of each panel in bold red letters. Colour shading displays how these reference values are distributed in terms of percentage in 56 combinations produced by seven synoptic-scale convective regimes and eight MJO phases. For the combined influence of OLR regimes and MJO phases, the OLR field from the first ensemble member of ERA5 is used [Colour figure can be viewed at wileyonlinelibrary.com]

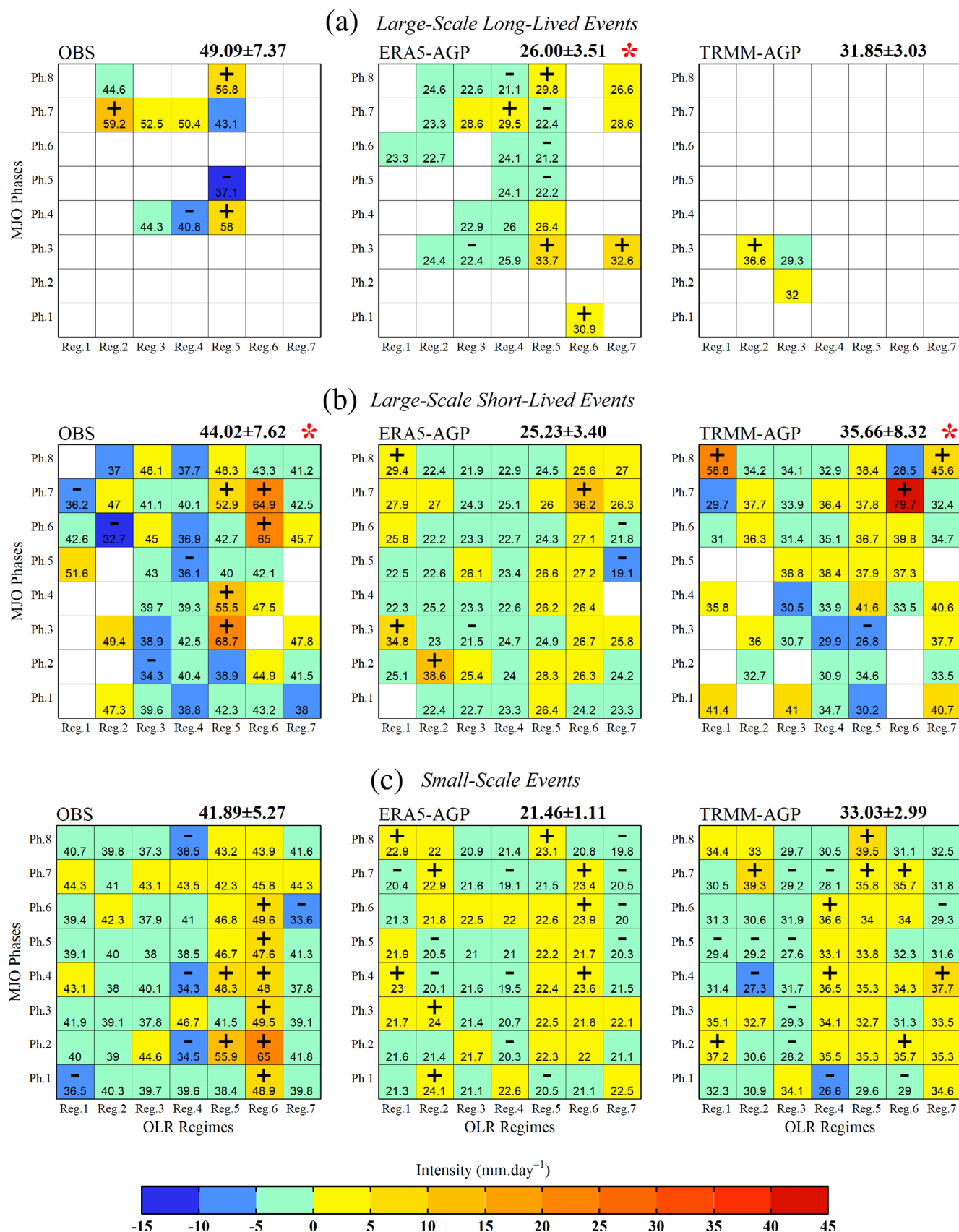


FIGURE 14 Legend on next page.

to all datasets (Figure 13b); (2) regime #3 with phase #3 in OBS and TRMM for 6% of days, although this signal is not identified in ERA5 (Figure 13b). Finally, days associated with small-scale extreme events are nearly equiprobable in almost all 56 concomitance classes. They appear slightly more frequently in regime #3 under moderate and wet MJO phases (Figure 13c).

Figure 14 displays the intensity of rainfall extremes during the combined influence of OLR regimes and MJO phases. In OBS, days associated with large-scale long-lived events are more intense in regime #5 occurring with MJO phases #4 and #8, with an average intensity of 56.8 mm day^{-1} (above one standard deviation: see, OBS panel in Figure 14a). For the days of large-scale short-lived events, all datasets show increased intensity when regime #5 is associated with all moderate and wet MJO phases (Figure 14b). Similar patterns appear in the intensity of small-scale extremes (see regimes #5–6 and their associations with most MJO phases in Figure 14c). This association seems coherent, as the MJO is known as a tropical mode of variability and regime #6 materializes strong tropical temperate connections, favoured by

sustained convective activity in the Tropics that help convection extend southwards over South Africa (Macron et al., 2014) (Figure S2). Our results show that 11%–16% of days associated with small-scale events occur in regime #6. Thus, small-scale extreme events with extremely high intensity can be anticipated when regime #6 coincides with strong MJO activity. The analysis presented in sections 4.1–4.3 is also provided for NN fields of ERA5 and TRMM in Figures S8–S13.

4.4 | Risk assessment at combined influence of synoptic and intraseasonal variability

To assess the risks of occurrence of extremes under different combinations of OLR regimes and MJO phases, we use a RR assessment (cf., section 2.3; Figure 15). Only regimes #3, #4 and #5 are presented here since the highest number of extremes occur in these regimes (section 4.1). The RR is then provided for each regime for dry (#1–2), moderate (#3–5) and wet phases (#6–8) of the MJO, as these groups

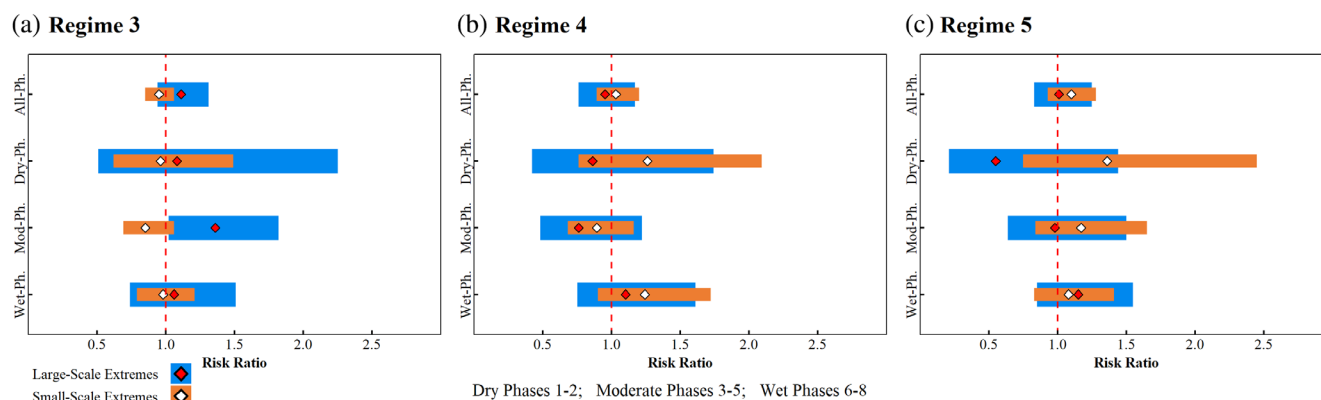


FIGURE 15 Estimated risk ratio for the P_F scenario, that is, the active MJO days (Amplitude >1.0 RMM) in each regime computed with respect to the P_{CF} scenario, that is, all days when MJO does not represent any phase (Amplitude <1.0 RMM) in respective regime provided explicitly for regime #3 (a), regime #4 (b) and regime #5 (c). For each regime, the risk ratio is computed by considering dry (i.e., phases #1–2), moderate (i.e., phases #3–5) and wet (i.e., phases #6–8), phases of the MJO. The blue stripes with red symbols in each panel represent risk ratio for large-scale extremes, whereas brown stripes with white symbols represent small-scale extremes. The horizontal expansion of stripes represents the minimum and maximum limits of the 95% confidence intervals. The symbols represent the numerical position of the risk ratio computed at $p = 0.05$. $RR = 1.0$ corresponds to an equiprobable risk of occurrence of extremes during P_F scenario (with MJO influence) or during P_{CF} scenario (without MJO influence). A risk ratio above or below 1.0 can be interpreted with a factor, for instance, 0.2, 0.4 and 0.6 indicate a 20%, 40% and 60% higher risk of occurrence of extremes during P_F scenario as compared to the P_{CF} scenario or vice versa if below 1.0 [Colour figure can be viewed at wileyonlinelibrary.com]

FIGURE 14 Same as Figure 13, but for intensity, except that the data is presented in terms of anomaly, computed with respect to the average value calculated by considering all OLR regimes and MJO phases (displayed in the top-right corner of each panel) whereas raw values are overlaid. The “+” and “–” symbols indicate the cells in which intensity differed from the $+1.0$ or -1.0 standard deviation, respectively [Colour figure can be viewed at wileyonlinelibrary.com]

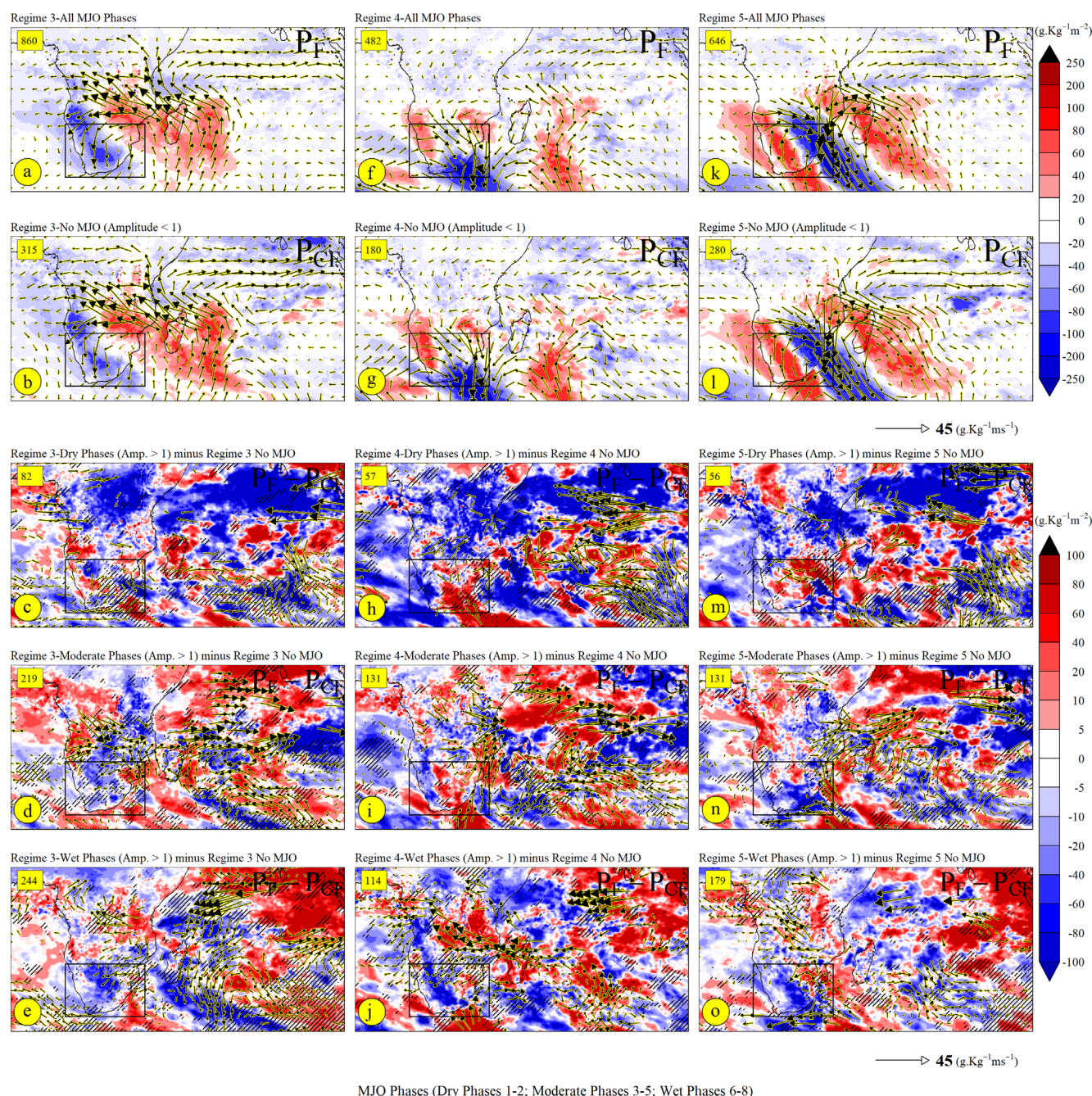


FIGURE 16 Set of six panels in top display the composite anomalies of vertically integrated moisture flux divergence ($\text{g kg}^{-1} \text{m}^{-2}$) and moisture flux ($\text{g kg}^{-1} \text{ms}^{-1}$) at 850 hPa in each P_F and P_{CF} scenario during regime #3 (a, b), regime #4 (f, g) and regime #5 (k, l), respectively, where only those anomalies are shown which are significant at 95% confidence level according to the one-tailed Student's t test. Anomalies are computed with respect to the climatology of NDJF from 1979 to 2015. Set of nine panels in bottom represent the differences between composite anomalies produced by considering those days in each set of phases (dry, moderate and wet phases) when amplitude >1.0 RMM and when MJO does not represent any phase (i.e., P_F minus P_{CF}) for regime #3 (c–e), for regime #4 (h–j) and for regime #5 (m–o). Stippling indicates the anomalies are significant according to two-tailed Student's t test at $p < 0.1$ while only significant fluxes are shown using wind barbs. The reference values in the upper-right corner indicate the number in of days in each composite while the black rectangle represents the area of interest, i.e., South Africa [Colour figure can be viewed at [wileyonlinelibrary.com](https://onlinelibrary.wiley.com/doi/10.1002/joc.8059)]

of contiguous phases are also found to be coherent and homogeneous in terms of rainfall extremes (section 4.2). RR is computed for each set of combinations when MJO is

active (P_F : Amplitude >1.0 RMM) with respect to all days when MJO does not represent any phase (P_{CF} : Amplitude <1.0 RMM) and is provided here only for OBS.

Regime #3 is associated with a RR of about 1.35 for the days associated with large-scale extremes when MJO is active, regardless of the phase with respect to the days when MJO is not present in this regime (Figure 15a). These differences are coherent with slightly weaker negative anomalies of VIMD and easterly moisture flux (Figure 16a,b). Further, in regime #3, the RR for large-scale extremes was found nearly 1.0 with wet and dry phases of MJO indicating that the occurrence of such extremes is equiprobable either with or without MJO. In regime #3, we note a RR of 1.36 with a confidence interval of 1.02–1.82 suggesting a 36% increase in the risk of occurrence of large-scale extremes with moderate phases of MJO as compared to when MJO is not active (Figure 15a). It may seem contradictory because the wet phases are known to favour convection over southern Africa. It is because RR is sensitive to the sample size. For instance, OBS data identified 70 days associated with large-scale extremes in regime #3 where 49 days were found when MJO show a phase with amplitude above 1.0 RMM and only 21 days when MJO does not show any phase. Among these 49 days, 25 days were associated with moderate phases of the MJO in a sample size of 219 days while 21 days occur during a substantially higher sample size of 315 days when MJO was not active with any phase. It is also worth noting that during regime #3 and moderate phases of the MJO, the occurrence of small-scale extremes was also higher as compared to other combinations as this signal is not only identified by AGP fields of ERA5 and TRMM but also with their NN fields as well (Figures 13 and S12). Figure 16c–e indicates that the differences in terms of convergence over South Africa are higher when MJO is active with the respective set of phases. For further clarification, we provide the composite anomalies of VIMD and moisture fluxes during regime #3 with moderate phases of the MJO (see Figure S14). Figure 16a,b shows that the moisture is diverging toward the northwest and over western parts of South Africa creating a regime structure while if we consider only those days when MJO is active with moderate phases (as shown in Figure S14), convergence extends on a larger region with higher strength while the moisture flux is more inward toward South Africa thus resulting in a higher number of large-scale extremes thereby confirming the RR result.

Figure 15b indicates the risk of occurrence of large-scale extremes is higher when MJO is inactive during regime #4 (i.e., P_{CF} scenario). However, this is not the case with wet phases of the MJO during regime #4, here we note a risk ratio of about 1.10 suggesting a 10% higher risk of occurrence of large-scale extremes (Figure 15b). Indo-Pacific composites of MJO circulation reveal that moisture flux anomalies are directed away from Africa during phases #2–4, and toward Africa during phases

#6–8 (Wheeler & Hendon, 2004). Our results confirm this as the differences in terms of divergence (convergence) are higher in regime #4 with dry and moderate (wet) phases of the MJO and these synoptic behaviours in terms of VIMD and moisture flux anomalies over South Africa are accurately mimicked by the risk ratio assessment (Figure 16h–j).

Like regime #4, the risk of occurrence of large-scale extremes in regime #5 is also higher without the influence of MJO (during P_{CF} scenario) when computed for the active MJO days of dry phases with respect to all days when MJO does not show any phase in regime #5 (Figure 15c). The differences in composite anomalies also suggest dry conditions during dry phases of the MJO over South Africa (Figure 16m). However, during regime #5 and wet phases of MJO, we note a RR of about 1.15 with a confidence interval between 0.85 and 1.55 suggesting a risk of occurrence of large-scale extremes is 15% higher with the MJO influence and even more if we consider the upper bound of the confidence interval. Moisture flux anomalies also suggest the difference is higher in terms of convergence over South Africa (Figure 16o). During all three regimes with different set of MJO phases, the risk of occurrence of small-scale extremes remains equiprobable either with or without the MJO activity. This suggests that MJO plays an important role in modulating the number of days associated with large-scale extremes.

The association between MJO phases and synoptic regimes works well mostly for regime #5 this confirms the results of Hart et al. (2013) according to which TTTs tend to be more intense, that is, bring more rainfall, when they occur during the wet phase of the MJO. The dry phases act to weaken them and decrease associated rainfall amounts. This translates into a different probability to exceed the local 90th percentile thresholds, hence a change in the RR metric. The results obtained from RR metric are quantitative and statistically significant but physical mechanisms studied here result in weak statistical significance (but not insignificant), confirming the results of RR by showing some interesting signals. The uncertainties in the physical mechanisms studied here may be due to the biases in the reanalysis and shorter sample size. Here we propose further aspects to extend this study by (1) considering a larger sample size; (2) using different reanalysis products to be sure if the signals are like ERA5; (3) exploring dynamical perspective using the strength of MJO amplitude; (4) investigating teleconnections with other regions in the perspective of the combined influence of synoptic regimes and MJO phases. Characterization of extremes for the region was never done before; this study fills this gap and by characterizing extremes according to their properties thus opening new dimensions for further research.

5 | CONCLUSIONS AND DISCUSSION

In Part I, we introduced a novel typology of rainfall extremes, accounting for their spatial extensions and disentangling large- and small-scale extreme events. Here, we attempt to investigate the variability of two types of rainfall extremes, first at interannual (IV: 2–8 years) and quasi-decadal (QDV: 8–13 years) timescales of variability, which are associated with ENSO and IPO, respectively (Dieppois et al., 2016, 2019; Pohl et al., 2018). Changes in the occurrence of rainfall extremes are next analysed at subseasonal (synoptic and intraseasonal) timescales. They are, respectively, related to short-lived disturbances either related to tropical convection, mid-latitude dynamics or interactions between both (Fauchereau et al., 2009; Hart et al., 2013; Macron et al., 2014, 2016) and to the regional influence of the MJO (Oettli et al., 2014; Pohl et al., 2007). For all timescales, risk ratio assessments are provided, to quantify the change in the probability for either small-scale or large-scale extremes to occur. To our knowledge, such quantifications of rainfall extremes have never been carried out for the region.

We first explore the link between extremes, either large or small scales, and global SSTs. The different ocean basins have substantially contrasted results with large- and small-scale extremes. This suggests the adequacy of the method used in Part I to characterize South African rainfall extremes as we speculated that large-scale circulations or modes of variability have a greater influence on the occurrence of large-scale extremes. We note that: (1) La Niña conditions favour overall wet conditions in South Africa, including an increased occurrence of rainfall extremes; (2) the number of days associated with large-scale extremes and contribution of total rainfall is related to warmer SSTs in the North Atlantic, while the relationship with warmer Indian Ocean and tropical South Atlantic appears as statistically independent of the state of ENSO; (3) the contribution of large- and small-scale extremes to total rainfall is greater during El Niño, despite generally drier conditions during these years.

At low frequencies (IV and QDV), a risk ratio assessment suggests that the probability of extremes varies with the changing magnitude of IV and QDV timescales, primarily associated with ENSO and IPO, respectively. At the IV timescale, the number of large-scale extremes and the total rainfall associated with small-scale extremes is much more frequent when this timescale lies in a strong positive phase, i.e., $>+0.5$ standard deviation. During these strong positive IV phases, we note a 400% rise in the probability of large-scale extremes as compared to the strong negative IV phases. This is consistent with the strong La Niña episodes in the Pacific SSTs, where

interannual variations play a primary role in shaping rainfall variability in South Africa. No substantial increment in the risk ratio is noted when computed for strong positive phases of the QDV timescale compared to strong negative phases. Considering these results, it is conceivable that the whole statistical distribution of daily rainfall extremes is strongly related to rainfall variations at the IV timescale and weak but significant on QDV timescale. These findings may play an important role in promoting multiyear seamless forecasts of rainfall extremes since they identify the modes of climate variability that drive part of their variability at both the IV and QDV timescales.

At the subseasonal timescales, days associated with large-scale events occur largely during synoptic regimes #3–5 (describing the precursors and then the mature phases of continental TTT systems), whereas small-scale extremes are nearly equiprobable during all regimes, except for regime #3, which shows slightly higher numbers of such extremes. In terms of intraseasonal variability, MJO phases #1–2, #3–5 and #6–8 are three coherent and homogeneous groups which are, respectively, associated with weak, moderate and high numbers of both types of extremes for South African rainfall. Previous studies suggested that the intensity of TTT events (i.e., their corresponding rainfall amounts) is increased during phase #6 and decreased in phase #1, even though TTT occurrence is not statistically modified by MJO phases (Hart et al., 2013). Our results related to regime #5 corroborate the results found in the literature and extend them to rainfall extremes.

In Part I, we noted that the large-scale extremes are spatially coherent and organized events, bringing more than half of total seasonal rainfall during just 8 ± 5 days season⁻¹. In this study, we find that around 75% of days associated with large-scale extreme events occur in regimes #3–5 which are characterized as early to mature TTT regimes. Thus, our results support the argument made by Hart et al. (2013) “that a single extreme event has the potential to drastically alter the seasonal rainfall total.” The extensive characterization of rainfall extremes carried out in this study is crucial in promoting long-term multiyear seamless forecasts for the region on one hand, and subseasonal operational forecasts on the other hand.

We investigate here the intraseasonal variability of rainfall extremes separately at low frequency and subseasonal timescales. It would be ideal to consider these timescales together, to analyse climate variability according to a real continuum of scales. This would include climate change, with expected changes in the rainfall extremes due to the Clausius-Clapeyron scaling relating air temperature to its humidity (Betts & Harshvardhan., 1987; Kharin et al., 2007; Muller et al., 2011; Pohl et al., 2017). The interdecadal timescale could also modify the changes in the intensity and

occurrence of rainfall extremes, from one decade to another, thereby influencing the changes that the region will experience in the coming decades. Observational datasets may be too short to perform such analyses of slowly changing modes of variability or mechanisms, hence the need for long model simulations. However, current climate models are mostly based on parameterized atmospheric convection, and convection-permitting simulations may be needed to better ascertain the influence of interdecadal variability on rainfall extremes (Jackson et al., 2020; Kendon et al., 2017, 2019; Senior et al., 2021). The question of their seamless predictability is also important because these events may be considered as those more likely to lead to strong impacts. Hence the need to develop a seamless prediction tool for rainfall extremes, and more generally, high-impact events over southern Africa and even Africa as a whole.

AUTHOR CONTRIBUTIONS

Asmat Ullah: Conceptualization; formal analysis; investigation; methodology; validation; visualization; writing – original draft. **Benjamin Pohl:** Conceptualization; funding acquisition; resources; supervision; writing – review and editing. **Julien Pergaud:** Data curation; resources; software; supervision. **Bastien Dieppo:** Conceptualization; data curation; writing – review and editing. **Mathieu Rouault:** Conceptualization; data curation; writing – review and editing.

ACKNOWLEDGEMENTS

This work is part of the I-SITE Bourgogne Franche-Comté Junior Fellowship IMVULA (Grant No. AAP2-JF-06), and the Alliance Programme 2020 (Grant No. 608081922), co-funded by the British Council and Campus-France. It was also supported by the NRF SARCHI chair on “modeling ocean-atmosphere-land interactions” and the Nansen Tutu Centre for Marine studies. Two anonymous reviewers are thanked for their constructive comments that helped us to improve the quality of the manuscript. Calculations were performed using HPC resources from DNUM CCUB (Centre de Calcul de l'Université de Bourgogne). The authors dedicate this work to Professor Mathieu Rouault who passed away when this paper was still in progress.

ORCID

Asmat Ullah  <https://orcid.org/0000-0002-3453-0347>

Benjamin Pohl  <https://orcid.org/0000-0002-9339-797X>

REFERENCES

- Betts, A.K. & Harshvardhan. (1987) Thermodynamic constraint on the cloud liquid water feedback in climate models. *Journal of Geophysical Research: Atmospheres*, 92(D7), 8483–8485. Available from: <https://doi.org/10.1029/JD092ID07P08483>
- Blamey, R.C. & Reason, C.J.C. (2013) The role of mesoscale convective complexes in southern Africa summer rainfall. *Journal of Climate*, 26(5), 1654–1668. Available from: <https://doi.org/10.1175/JCLI-D-12-00239.1>
- Conway, D., Dalin, C., Landman, W.A. & Osborn, T.J. (2017) Hydropower plans in eastern and southern Africa increase risk of concurrent climate-related electricity supply disruption. *Nature Energy*, 2(12), 946–953. Available from: <https://doi.org/10.1038/s41560-017-0037-4>
- Conway, D., Van Garderen, E.A., Deryng, D., Dorling, S., Krueger, T., Landman, W. et al. (2015) Climate and southern Africa's water-energy-food nexus. *Nature Climate Change*, 5(9), 837–846. Available from: <https://doi.org/10.1038/nclimate2735>
- Crétat, J., Richard, Y., Pohl, B., Rouault, M., Reason, C. & Fauchereau, N. (2012) Recurrent daily rainfall patterns over South Africa and associated dynamics during the core of the austral summer. *International Journal of Climatology*, 32(2), 261–273. Available from: <https://doi.org/10.1002/joc.2266>
- Desbiolles, F., Howard, E., Blamey, R.C., Barimalala, R., Hart, N.C. G. & Reason, C.J.C. (2020) Role of ocean mesoscale structures in shaping the Angola-Low pressure system and the southern Africa rainfall. *Climate Dynamics*, 54(7–8), 3685–3704. Available from: <https://doi.org/10.1007/s00382-020-05199-1>
- Dieppo, B., Pohl, B., Crétat, J., Eden, J., Sidibe, M., New, M. et al. (2019) Southern African summer-rainfall variability, and its teleconnections, on interannual to interdecadal timescales in CMIP5 models. *Climate Dynamics*, 53(5–6), 3505–3527. Available from: <https://doi.org/10.1007/s00382-019-04720-5>
- Dieppo, B., Pohl, B., Rouault, M., New, M., Lawler, D. & Keenlyside, N. (2016) Interannual to interdecadal variability of winter and summer southern African rainfall, and their teleconnections. *Journal of Geophysical Research*, 121, 6215–6239. Available from: <https://doi.org/10.1002/2015JD024576>
- Dieppo, B., Rouault, M. & New, M. (2015) The impact of ENSO on Southern African rainfall in CMIP5 ocean atmosphere coupled climate models. *Climate Dynamics*, 45(9–10), 2425–2442. Available from: <https://doi.org/10.1007/s00382-015-2480-x>
- Donald, A., Meinke, H., Power, B., Maia, A.H.N., Wheeler, M.C., White, N. et al. (2006) Near-global impact of the Madden-Julian Oscillation on rainfall. *Geophysical Research Letters*, 33(9), 6–9. Available from: <https://doi.org/10.1029/2005GL025155>
- Donat, M.G., Lowry, A.L., Alexander, L.V., O'Gorman, P.A. & Maher, N. (2016) More extreme precipitation in the world's dry and wet regions. *Nature Climate Change*, 6(5), 508–513. Available from: <https://doi.org/10.1038/NCLIMATE2941>
- Engelbrecht, C.J., Engelbrecht, F.A. & Dyson, L.L. (2013) High-resolution model-projected changes in mid-tropospheric closed-lows and extreme rainfall events over southern Africa. *International Journal of Climatology*, 33(1), 173–187. Available from: <https://doi.org/10.1002/joc.3420>
- Fauchereau, N., Pohl, B., Reason, C.J.C., Rouault, M. & Richard, Y. (2009) Recurrent daily OLR patterns in the Southern Africa/Southwest Indian ocean region, implications for South African rainfall and teleconnections. *Climate Dynamics*, 32(4), 575–591. Available from: <https://doi.org/10.1007/s00382-008-0426-2>
- Favre, A., Hewitson, B., Lennard, C., Cerezo-Mota, R. & Tadross, M. (2013) Cut-off lows in the South Africa region and their contribution to precipitation. *Climate Dynamics*, 41(9–10), 2331–2351. Available from: <https://doi.org/10.1007/s00382-012-1579-6>

- Fitchett, J.M. & Grab, S.W. (2014) A 66-year tropical cyclone record for south-east Africa: temporal trends in a global context. *International Journal of Climatology*, 34(13), 3604–3615. Available from: <https://doi.org/10.1002/joc.3932>
- Grimm, A.M. (2019) Madden–Julian Oscillation impacts on South American summer monsoon season: precipitation anomalies, extreme events, teleconnections, and role in the MJO cycle. *Climate Dynamics*, 53(1–2), 907–932. Available from: <https://doi.org/10.1007/s00382-019-04622-6>
- Grimm, A.M. & Reason, C.J.C. (2011) Does the South American monsoon influence African rainfall? *Journal of Climate*, 24(4), 1226–1238. Available from: <https://doi.org/10.1175/2010JCLI3722.1>
- Grimm, A.M. & Reason, C.J.C. (2015) Intraseasonal teleconnections between South America and South Africa. *Journal of Climate*, 28(23), 9489–9497. Available from: <https://doi.org/10.1175/JCLI-D-15-0116.1>
- Hart, N.C.G., Reason, C.J.C. & Fauchereau, N. (2010) Tropical–extratropical interactions over southern Africa: three cases of heavy summer season rainfall. *Monthly Weather Review*, 138(7), 2608–2623. Available from: <https://doi.org/10.1175/2010MWR3070.1>
- Hart, N.C.G., Reason, C.J.C. & Fauchereau, N. (2013) Cloud bands over southern Africa: seasonality, contribution to rainfall variability and modulation by the MJO. *Climate Dynamics*, 41(5–6), 1199–1212. Available from: <https://doi.org/10.1007/s00382-012-1589-4>
- Hersbach, H., Bell, B., Berrisford, P., Hirahara, S., Horányi, A., Muñoz-Sabater, J. et al. (2020) The ERA5 global reanalysis. *Quarterly Journal of the Royal Meteorological Society*, 146(730), 1999–2049. Available from: <https://doi.org/10.1002/qj.3803>
- Hoell, A. & Cheng, L. (2018) Austral summer Southern Africa precipitation extremes forced by the El Niño–Southern Oscillation and the subtropical Indian Ocean dipole. *Climate Dynamics*, 50(9–10), 3219–3236. Available from: <https://doi.org/10.1007/s00382-017-3801-z>
- Huang, B., Thorne, P.W., Banzon, V.F., Boyer, T., Chepurin, G., Lawrimore, J.H. et al. (2017) Extended reconstructed sea surface temperature, version 5 (ERSSTv5): upgrades, validations, and intercomparisons. *Journal of Climate*, 30(20), 8179–8205. Available from: <https://doi.org/10.1175/JCLI-D-16-0836.1>
- Huffman, G.J., Adler, R.F., Bolvin, D.T., Gu, G., Nelkin, E.J., Bowman, K.P. et al. (2007) The TRMM multisatellite precipitation analysis (TMPA): quasi-global, multiyear, combined-sensor precipitation estimates at fine scales. *Journal of Hydrometeorology*, 8(1), 38–55. Available from: <https://doi.org/10.1175/JHM560.1>
- Jackson, L.S., Finney, D.L., Kendon, E.J., Marsham, J.H., Parker, D. J., Stratton, R.A. et al. (2020) The effect of explicit convection on couplings between rainfall, humidity, and ascent over Africa under climate change. *Journal of Climate*, 33(19), 8315–8337. Available from: <https://doi.org/10.1175/JCLI-D-19-0322.1>
- James, R., Hart, N.C.G., Munday, C., Reason, C.J.C. & Washington, R. (2020) Coupled climate model simulation of tropical–extratropical cloud bands over southern Africa. *Journal of Climate*, 33(19), 8579–8602. Available from: <https://doi.org/10.1175/JCLI-D-19-0731.1>
- Kalnay, E., Kanamitsu, M., Kistler, R., Collins, W., Deaven, D., Gandin, L. et al. (1996) The NCEP/NCAR 40-year reanalysis project. *Bulletin of the American Meteorological Society*, 77(3), 437–472.
- Kendon, E.J., Ban, N., Roberts, N.M., Fowler, H.J., Roberts, M.J., Chan, S.C. et al. (2017) Do convection-permitting regional climate models improve projections of future precipitation change? *Bulletin of the American Meteorological Society*, 98(1), 79–93. Available from: <https://doi.org/10.1175/BAMS-D-15-0004.1>
- Kendon, E.J., Stratton, R.A., Tucker, S., Marsham, J.H., Berthou, S., Rowell, D.P. et al. (2019) Enhanced future changes in wet and dry extremes over Africa at convection-permitting scale. *Nature Communications*, 10(1), 1794. Available from: <https://doi.org/10.1038/s41467-019-09776-9>
- Kharin, V.V., Zwiers, F.W., Zhang, X. & Hegerl, G.C. (2007) Changes in temperature and precipitation extremes in the IPCC ensemble of global coupled model simulations. *Journal of Climate*, 20(8), 1419–1444. Available from: <https://doi.org/10.1175/JCLI4066.1>
- Lyon, B. & Mason, S.J. (2007) The 1997–98 summer rainfall season in southern Africa. Part I: observations. *Journal of Climate*, 20(20), 5134–5148. Available from: <https://doi.org/10.1175/JCLI4225.1>
- Macron, C., Pohl, B., Richard, Y. & Bessafi, M. (2014) How do tropical temperate troughs form and develop over southern Africa? *Journal of Climate*, 27(4), 1633–1647. Available from: <https://doi.org/10.1175/JCLI-D-13-00175.1>
- Macron, C., Richard, Y., Garot, T., Bessafi, M., Pohl, B., Ratiarison, A. et al. (2016) Intraseasonal rainfall variability over Madagascar. *Monthly Weather Review*, 144(5), 1877–1885. Available from: <https://doi.org/10.1175/MWR-D-15-0077.1>
- Madden, R.A. & Julian, P.R. (1994) Observations of the 40–50-day tropical oscillation—a review. *Monthly Weather Review*, 122, 814–837. Available from: [https://doi.org/10.1175/1520-0493\(1994\)122<0814:OOTDTP>2.0.CO;2](https://doi.org/10.1175/1520-0493(1994)122<0814:OOTDTP>2.0.CO;2)
- Malherbe, J., Dieppois, B., Maluleke, P., Van Staden, M. & Pillay, D.L. (2016) South African droughts and decadal variability. *Natural Hazards*, 80(1), 657–681. Available from: <https://doi.org/10.1007/s11069-015-1989-y>
- Malherbe, J., Engelbrecht, F.A., Landman, W.A. & Engelbrecht, C. J. (2012) Tropical systems from the southwest Indian Ocean making landfall over the Limpopo River Basin southern Africa: a historical perspective. *International Journal of Climatology*, 32(7), 1018–1032. Available from: <https://doi.org/10.1002/joc.2320>
- Malherbe, J., Landman, W.A. & Engelbrecht, F.A. (2014) The bi-decadal rainfall cycle, southern annular mode and tropical cyclones over the Limpopo River basin, southern Africa. *Climate Dynamics*, 42(11–12), 3121–3138. Available from: <https://doi.org/10.1007/s00382-013-2027-y>
- Mason, S.J., Goddard, L., Graham, N.E., Yulaeva, E., Sun, L. & Arkin, P.A. (1999) The IRI seasonal climate prediction system. In: *WRPMD 1999: preparing for the 21st century*. Reston, VA: ASCE.
- Mason, S.J. & Joubert, A.M. (1997) Simulated changes in extreme rainfall over southern Africa. *International Journal of Climatology*, 17(3), 291–301. Available from: [https://doi.org/10.1002/\(sici\)1097-0088\(19970315\)17:3<291::aid-joc120>3.3.co;2-t](https://doi.org/10.1002/(sici)1097-0088(19970315)17:3<291::aid-joc120>3.3.co;2-t)
- Muller, C.J., O’Gorman, P.A. & Back, L.E. (2011) Intensification of precipitation extremes with warming in a cloud-resolving model. *Journal of Climate*, 24(11), 2784–2800. Available from: <https://doi.org/10.1175/2011JCLI3876.1>

- Nicholson, S.E. & Kim, J. (1997) The relationship of the El Niño–Southern Oscillation to African rainfall. *International Journal of Climatology*, 17(2), 117–135. Available from: [https://doi.org/10.1002/\(SICI\)1097-0088\(199702\)17:2<117::AID-JOC84>3.0.CO;2-O](https://doi.org/10.1002/(SICI)1097-0088(199702)17:2<117::AID-JOC84>3.0.CO;2-O)
- Oettli, P., Tozuka, T., Izumo, T., Engelbrecht, F.A. & Yamagata, T. (2014) The self-organizing map, a new approach to apprehend the Madden–Julian Oscillation influence on the intraseasonal variability of rainfall in the southern African region. *Climate Dynamics*, 43(5–6), 1557–1573. Available from: <https://doi.org/10.1007/s00382-013-1985-4>
- Paciorek, C.J., Stone, D.A. & Wehner, M.F. (2018) Quantifying statistical uncertainty in the attribution of human influence on severe weather. *Weather and Climate Extremes*, 20, 69–80. Available from: <https://doi.org/10.1016/j.wace.2018.01.002>
- Pascale, S., Pohl, B., Kapnick, S.B. & Zhang, H. (2019) On the Angola low interannual variability and its role in modulating ENSO effects in southern Africa. *Journal of Climate*, 32(15), 4783–4803. Available from: <https://doi.org/10.1175/JCLI-D-18-0745.1>
- Pinto, I., Lennard, C., Tadross, M., Hewitson, B., Dosio, A., Nikulin, G. et al. (2016) Evaluation and projections of extreme precipitation over southern Africa from two CORDEX models. *Climatic Change*, 135(3–4), 655–668. Available from: <https://doi.org/10.1007/s10584-015-1573-1>
- Pohl, B., Dieppois, B., Crétat, J., Lawler, D. & Rouault, M. (2018) From synoptic to interdecadal variability in southern African rainfall: toward a unified view across time scales. *Journal of Climate*, 31(15), 5845–5872. Available from: <https://doi.org/10.1175/JCLI-D-17-0405.1>
- Pohl, B., Fauchereau, N., Reason, C.J.C. & Rouault, M. (2010) Relationships between the Antarctic oscillation, the Madden–Julian Oscillation, and ENSO, and consequences for rainfall analysis. *Journal of Climate*, 23(2), 238–254. Available from: <https://doi.org/10.1175/2009JCLI2443.1>
- Pohl, B., Fauchereau, N., Richard, Y., Rouault, M. & Reason, C.J.C. (2009) Interactions between synoptic, intraseasonal and interannual convective variability over southern Africa. *Climate Dynamics*, 33(7–8), 1033–1050. Available from: <https://doi.org/10.1007/s00382-008-0485-4>
- Pohl, B., Macron, C. & Monerie, P.A. (2017) Fewer rainy days and more extreme rainfall by the end of the century in southern Africa. *Scientific Reports*, 7, 6–12. Available from: <https://doi.org/10.1038/srep46466>
- Pohl, B., Richard, Y. & Fauchereau, N. (2007) Influence of the Madden–Julian Oscillation on southern African summer rainfall. *Journal of Climate*, 20(16), 4227–4242. Available from: <https://doi.org/10.1175/JCLI4231.1>
- Pomposi, C., Funk, C., Shukla, S., Harrison, L. & Magadzire, T. (2018) Distinguishing southern Africa precipitation response by strength of El Niño events and implications for decision-making. *Environmental Research Letters*, 13(7), 074015. Available from: <https://doi.org/10.1088/1748-9326/aacc4c>
- Puaud, Y., Pohl, B., Fauchereau, N., Macron, C. & Beltrando, G. (2017) Climate co-variability between South America and southern Africa at interannual, intraseasonal and synoptic scales. *Climate Dynamics*, 48(11–12), 4029–4050. Available from: <https://doi.org/10.1007/S00382-016-3318-X/FIGURES/13>
- Rapolaki, R.S., Blamey, R.C., Hermes, J.C. & Reason, C.J.C. (2019) A classification of synoptic weather patterns linked to extreme rainfall over the Limpopo River basin in southern Africa. *Climate Dynamics*, 53(3–4), 2265–2279. Available from: <https://doi.org/10.1007/s00382-019-04829-7>
- Rapolaki, R.S., Blamey, R.C., Hermes, J.C. & Reason, C.J.C. (2020) Moisture sources associated with heavy rainfall over the Limpopo River basin, southern Africa. *Climate Dynamics*, 55(5–6), 1473–1487. Available from: <https://doi.org/10.1007/s00382-020-05336-w>
- Reason, C.J.C. (2001) Subtropical Indian Ocean SST dipole events and southern African rainfall. *Geophysical Research Letters*, 28, 2225–2227. Available from: <https://doi.org/10.1029/2000GL012735>
- Reason, C.J.C. & Jagadheesha, D. (2005) A model investigation of recent ENSO impacts over southern Africa. *Meteorology and Atmospheric Physics*, 89(1–4), 181–205. Available from: <https://doi.org/10.1007/s00703-005-0128-9>
- Reason, C.J.C. & Keibel, A. (2004) Tropical cyclone Eline and its unusual penetration and impacts over the southern Africa mainland. *Weather and Forecasting*, 19(5), 789–805. Available from: [https://doi.org/10.1175/1520-0434\(2004\)019<0789:TCEAIU>2.0.CO;2](https://doi.org/10.1175/1520-0434(2004)019<0789:TCEAIU>2.0.CO;2)
- Reason, C.J.C., Landman, W. & Tennant, W. (2006) Seasonal to decadal prediction of southern African climate and its links with variability of the Atlantic Ocean. *Bulletin of the American Meteorological Society*, 87(7), 941–955. Available from: <https://doi.org/10.1175/BAMS-87-7-941>
- Rouault, M., Florenchie, P., Fauchereau, N. & Reason, C.J.C. (2003) South east tropical Atlantic warm events and southern African rainfall. *Geophysical Research Letters*, 30(5), 1–4. Available from: <https://doi.org/10.1029/2002GL014840>
- Rouault, M. & Richard, Y. (2004) Intensity and spatial extension of drought in South Africa at different time scales. *Water SA*, 29(4), 489–500. Available from: <https://doi.org/10.4314/wsa.v29i4.5057>
- Rouault, M., White, S.A., Reason, C.J.C., Lutjeharms, J.R.E. & Jobard, I. (2002) Ocean–atmosphere interaction in the Agulhas current region and a South African extreme weather event. *Weather and Forecasting*, 17, 655–669. Available from: [https://doi.org/10.1175/1520-0434\(2002\)017<0655:OAIITA>2.0.CO;2](https://doi.org/10.1175/1520-0434(2002)017<0655:OAIITA>2.0.CO;2)
- Senior, C.A., Marsham, J.H., Berthou, S., Burgin, L.E., Folwell, S.S., Kendon, E.J. et al. (2021) Convection-permitting regional climate change simulations for understanding future climate and informing decision-making in Africa. *Bulletin of the American Meteorological Society*, 102(6), E1206–E1223. Available from: <https://doi.org/10.1175/BAMS-D-20-0020.1>
- Shongwe, M.E., Van Oldenborgh, G.J., Van Den Hurk, B.J.J.M., De Boer, B., Coelho, C.A.S. & Van Aalst, M.K. (2009) Projected changes in mean and extreme precipitation in Africa under global warming. Part I: southern Africa. *Journal of Climate*, 22(13), 3819–3837. Available from: <https://doi.org/10.1175/2009JCLI2317.1>
- Silvério, K.C. & Grimm, A.M. (2022) Southern African monsoon: intraseasonal variability and monsoon indices. *Climate Dynamics*, 58(3–4), 1193–1220. Available from: <https://doi.org/10.1007/s00382-021-05954-y>
- Thoithi, W., Blamey, R.C. & Reason, C.J.C. (2020) Dry spell frequencies, wet day counts and their trends across southern Africa during the summer rainy season. *Geophysical*

- Research Letters*, 48(5), 1–22. Available from: <https://doi.org/10.1029/2020GL091041>
- Todd, M. & Washington, R. (1999) Circulation anomalies associated with tropical-temperate troughs in southern Africa and the south west Indian Ocean. *Climate Dynamics*, 15(12), 937–951. Available from: <https://doi.org/10.1007/s003820050323>
- Todd, M.C., Washington, R. & Palmer, P.I. (2004) Water vapour transport associated with tropical-temperate trough systems over southern Africa and the southwest Indian Ocean. *International Journal of Climatology*, 24(5), 555–568. Available from: <https://doi.org/10.1002/joc.1023>
- Ullah, A., Pohl, B., Pergaud, J., Dieppois, B. & Rouault, M. (2022) Intraseasonal descriptors and extremes in South African rainfall. Part I: summer climatology and statistical characteristics. *International Journal of Climatology*, 42(9), 4538–4563. Available from: <https://doi.org/10.1002/JOC.7489>
- Vigaud, N., Pohl, B. & Cr  tat, J. (2012) Tropical-temperate interactions over southern Africa simulated by a regional climate model. *Climate Dynamics*, 39(12), 2895–2916. Available from: <https://doi.org/10.1007/s00382-012-1314-3>
- Washington, R. & Preston, A. (2006) Extreme wet years over southern Africa: role of Indian Ocean sea surface temperatures. *Journal of Geophysical Research: Atmospheres*, 111(D15), 15104. Available from: <https://doi.org/10.1029/2005JD006724>
- Washington, R. & Todd, M. (1999) Tropical-temperate links in southern African and Southwest Indian Ocean satellite-derived daily rainfall. *International Journal of Climatology*, 19, 1601–1616. Available from: [https://doi.org/10.1002/\(SICI\)1097-0088\(19991130\)19:14<1601::AID-JOC407>3.0.CO;2-0](https://doi.org/10.1002/(SICI)1097-0088(19991130)19:14<1601::AID-JOC407>3.0.CO;2-0)
- Wheeler, M.C. & Hendon, H.H. (2004) An all-season real-time multivariate MJO index: development of an index for monitoring and prediction. *Monthly Weather Review*, 132(8), 1917–1932. Available from: [https://doi.org/10.1175/1520-0493\(2004\)132<1917:AARMMI>2.0.CO;2](https://doi.org/10.1175/1520-0493(2004)132<1917:AARMMI>2.0.CO;2)
- Zhang, C. (2005) Madden–Julian Oscillation. *Reviews of Geophysics*, 43(2), 1–36. Available from: <https://doi.org/10.1029/2004RG000158>

SUPPORTING INFORMATION

Additional supporting information can be found online in the Supporting Information section at the end of this article.

How to cite this article: Ullah, A., Pohl, B., Pergaud, J., Dieppois, B., & Rouault, M. (2023). Intraseasonal descriptors and extremes in South African rainfall. Part II: Summer teleconnections across multiple timescales. *International Journal of Climatology*, 1–29. <https://doi.org/10.1002/joc.8059>